Journal of the European Ceramic Society xxx (xxxx) xxx

Contents lists available at ScienceDirect

Journal of the European Ceramic Society

journal homepage: www.elsevier.com/locate/jeurceramsoc

BN nanosheets reinforced zirconia composites: An in-depth microstructural and mechanical study

C. Muñoz-Ferreiro [a,b,c,*], H. Reveron [c], T.C. Rojas [b], D.F. Reyes [d], S. Cottrino [c], P. Moreno [e], J. Prada-Rodrigo [e], A. Morales-Rodríguez [a], J. Chevalier [c], Á. Gallardo-López [a], R. Poyato [b]

[a] Dpto. de Física de la Materia Condensada, ICMS, CSIC-Universidad de Sevilla, Apdo. 1065, 41080 Sevilla, Spain
[b] Instituto de Ciencia de Materiales de Sevilla, ICMS, CSIC-Universidad de Sevilla, Avda. Américo Vespucio 49, 41092 Sevilla, Spain
[c] CNRS, INSA Lyon, Universite Claude Bernard Lyon 1, MATEIS, UMR5510, 69621 Villeurbanne, France
[d] University Research Institute on Electron Microscopy & Materials, (IMEYMAT), Universidad de Cádiz, Puerto Real, Cádiz 11510, Spain
[e] Grupo de Aplicaciones del Láser y Fotónica (ALF-USAL), Unidad de Excelencia en Luz y Materia Estructuradas (LUMES), Universidad de Salamanca, Pl. de la Merced s/n, 37008 Salamanca, Spain

ARTICLE INFO

Keywords:
Boron nitride nanosheets
Composite materials
Interfaces
R-curve
Crack bridging

ABSTRACT

This paper deals with the effect of hydroxylated boron nitride nanosheets (BNNS) incorporation on the microstructural and mechanical features of zirconia ceramics. Few-layered BNNS were synthesized via a simple hydroxide-assisted planetary ball milling exfoliation technique. 3 mol% yttria tetragonal zirconia polycrystal (3Y-TZP) with 2.5 vol% BNNS powders were prepared by an environmentally friendly process in water, and spark-plasma sintered at three temperatures to explore the in-situ reduction of the functionalized BNNS. An exhaustive study by (S)TEM techniques was performed to elucidate the influence of the sintering temperature on the matrix and the 3Y-TZP/BNNS interfaces, revealing that BNNS were homogeneously distributed throughout the matrix with an abrupt transition at 3Y-TZP/BNNS interfaces. BNNS effectively hindered slow crack growth, thus increasing the composite's crack growth resistance by about 30 %. A 1 MPa·m$^{1/2}$ rising R-curve was also induced by crack bridging.

1. Introduction

In the last decade, several studies have reported the enhancement of the mechanical, thermal or tribological properties of ceramics such as Si_3N_4 [1,2], AlN [3,4], Al_2O_3/YAG/YSZ [5] or Al_2O_3-ZrO_2 [6] when incorporating two-dimensional hexagonal boron nitride (2D-BN) as a second phase. The enhancement is a direct consequence of the excellent properties of this nanomaterial, also known as "white graphene" because of its structure analog to the one of graphene and its white color. These properties include high mechanical strength, excellent thermal conductivity, good lubrication properties and high oxidation resistance, sustaining temperatures up to 850 ºC [7]. Furthermore, in the case of boron nitride nanosheets (BNNS) -with a number of BN layers between 2 and 10- the good mechanical properties are maintained [2,7–9] and the onset of oxidation is only slightly increased with the increasing number of nanosheet layers [7].

Significant improvements of the bending strength and fracture toughness of ceramic composites incorporating 2D-BN have been reported for filler contents up to 2 wt% [1–6]. Lee et al. [6] measured a 20 % increase in K_{IC} on alumina toughened zirconia (ATZ) composites with the addition of 1 vol% BN nanoplatelets (BNNP). Reinforcing Si_3N_4 with 2 vol% BNNP also toughened the composite by almost 25 % when compared to the monolithic ceramic [1]. Similarly, Sun et al. [10] observed a 50 % increment in fracture toughness on fused silica composites when incorporating 1.5 wt% BNNS. Most studies on ceramic composites incorporating two-dimensional reinforcements only determine the fracture toughness of the materials, relating its enhancement to nanosheet pull-out or bridging [1,6,10–12]. Since these mechanisms activate as the fissure propagates, they may actually be promoting a rising crack growth resistance with crack extension (R-curve). Despite the great importance of R-curve evaluation in these composites, the works devoted to such analyses are very scarce on graphene reinforced ceramics [13–15] and, to the best of our knowledge, inexistent when considering 2D-BN as filler. Moreover, oxide ceramics suffer from a stress-assisted corrosion by water molecules, known as slow crack growth (SCG). The bending test conditions, such as the crosshead speed,

* Corresponding author at: Dpto. de Física de la Materia Condensada, ICMS, CSIC-Universidad de Sevilla, Apdo. 1065, 41080 Sevilla, Spain.
E-mail address: cmunoz7@us.es (C. Muñoz-Ferreiro).

https://doi.org/10.1016/j.jeurceramsoc.2024.02.002
Received 11 October 2023; Received in revised form 19 January 2024; Accepted 1 February 2024
Available online 4 February 2024

may influence fracture toughness results, since SCG is either controlled by the kinetics of the water-ceramic reaction or the water diffusion velocity to the crack tip [16]. Thus, it is important to determine to which extent SCG affects 2D-BN/ceramic composites to ensure a proper toughness evaluation.

Although a relative enhancement in the mechanical properties of these composites is often described, the toughening greatly depends on the features of the 2D material (thickness, lateral size or functionalization), its dispersion throughout the matrix and its orientation. High aspect ratio graphene nanosheets induce larger reinforcements in ceramic composites [12,13,17–19]. The use of uniaxial pressure during sintering promotes a preferential orientation of these 2D nanostructures, originating anisotropic properties. Wang et al. [19] observed negligible toughening in Al_2O_3-graphene composites when the crack front propagated parallel to the main plane of the reduced graphene oxide (rGO) nanosheets. In contrast, an increased K_{IC} was measured in the perpendicular direction. Moreover, a rising R-curve is also detected only when the crack front extends perpendicularly to the rGO main plane in 3Y-TZP [13] or 8Y-stabilized cubic zirconia (SCZ) [14] composites. Thus, a precise control of the powder processing and the sintering conditions is critical for the enhancement of the composite mechanical performance.

In order to achieve a complete optimization of the composite properties, the control of the microstructural features of the ceramic matrix is also essential. A decrease of the ceramic grain size has been reported for AlN [3,4], Al_2O_3 [11] or Si_3N_4 [20] matrices when increasing the BNNS content. On the contrary, increases in grain size and grain size distribution have been reported for 3Y-TZP [21] and zirconia toughened alumina (ZTA) [22] composites with boron nitride nanotubes (BNNT) as filler. Although it could be thought that the two BN nanostructures have a different effect on the grain size as consequence of their different intrinsic nature (1D for BNNT vs 2D for BNNS), these authors have related the grain growth to the formation of a liquid phase during sintering, related to the presence of residual metal catalysts [21] or elemental boron residue [22] in the BNNT. According to these authors, this liquid phase sintering generated a vitreous phase at the grain boundaries and triple junctions of the ceramic grains of the composites. Thus, an in-depth study of the nature of the ceramic grain boundary and triple points is essential.

Regarding the interfacial characteristics of ceramic composites with nanostructured BN, scarce studies have been devoted to their analysis despite their major influence on the composite properties. Specifically, the ceramic-filler bonding strength has been pointed out as a key factor for enhanced composite toughening [23]. Delamination and debonding of the outmost h-BN layers were observed on Si_3N_4/BNNS [2] and 3Y-TZP/BNNS [24] composites, suggesting that the ceramic-BNNS interfacial bonding was much stronger than the bonding between the individual h-BN layers. Nevertheless, no intergranular phase or diffusion layer was observed at the interface. Similarly, the strong chemical bonding of ceramic-filler interfaces achieved by spark plasma sintering (SPS) in a reducing atmosphere was suggested as responsible of the enhanced fracture toughness obtained in ceramic matrix (SiC or zirconia) composites with reduced graphene oxide (rGO) [12,25].

Among the synthesis techniques being used at present to obtain BNNS, the exfoliation from h-BN powder as parent material by ball milling stands out from other top-down approaches as liquid phase exfoliation [26], or bottom-up approaches as chemical vapor deposition (CVD), or solid-phase reaction [5], due to advantages as high yield, low cost and scalability. An exfoliation process for hydroxyl-functionalized BN nanoplatelets (BNNP) by a simple planetary ball milling of BN powders in the presence of sodium hydroxide was proposed by Lee et al. [27]. This process resulted in a high yield of 18 % of OH-BNNP that can be redispersed in various solvents and form stable suspensions. This would favor the preparation of a ceramic composite powder with an optimized BNNS dispersion using the most suitable solvent, resulting in the homogeneous distribution of the BNNS in the ceramic matrix, which is crucial in this type of composites. Furthermore, the hydroxyl-functionalization of the BNNS could also affect the interface with the ceramic matrix in SPSed BNNS composites, as the in-situ reduction of the OH-BNNS during spark plasma sintering in a reducing atmosphere could enhance the interaction of the BNNS with the zirconia matrix by generating a chemical bonding at the ceramic-filler interfaces. The in-situ reduction of GO to rGO during spark plasma sintering in a reducing atmosphere was pointed out as responsible of this bonding.

The aim of the present study is to investigate the effect of the incorporation of hydroxylated boron nitride nanosheets (BNNS) on the microstructural features and mechanical performance of zirconia composites. To that end, BNNS were obtained by a simple hydroxide assisted planetary ball milling exfoliation technique. The exfoliated BNNS were characterized by HR-TEM, TGA, XPS and Raman spectroscopy. The composite powders were prepared by a simple and environmentally friendly process in water, thanks to the enhanced stability of the BNNS suspensions and spark plasma sintered at three different temperatures in order to explore the in-situ reduction of the OH-BNNS. The microstructure of the sintered composites was analyzed by XRD, Raman spectroscopy, SEM and (S)TEM techniques. A meticulous study by HR-TEM, HAADF-STEM and X-EDS and EELS spectroscopies was performed to elucidate the influence of the sintering temperature on the 3Y-TZP/BNNS interfaces. To the best of our knowledge, this is the first time that such an exhaustive (S)TEM study of the BNNS-ceramic interfaces has been conducted. The composite mechanical properties were also examined. In particular, Young's modulus, Vickers hardness and fracture toughness were estimated, and crack growth resistance curves were evaluated. The crack-propagation path before failure and crack front after failure were analyzed in detail by SEM and grazing-incidence XRD to investigate the possible toughening mechanisms. Finally, the composite R-curve was also measured on a specimen impregnated in olive oil to determine the impact of slow crack growth on this type of materials.

2. Experimental procedure

2.1. Materials Processing

2.1.1. Synthesis and characterization of the BN Nanosheets

In this work, the BNNS exfoliation procedure proposed by Lee et al. [27] was selected as a simple and scalable way of producing large hydroxyl functionalized nanosheets with high yield. 2 g of h-BN powder (99.5 % purity, particle size $\leq$ 44 μm, Alfa Aesar, Kandel, Germany) were loaded into a 45 ml steel grinding container with 25 10-mm diameter steel balls, using a 50:1 balls-to-powder ratio. A 2 M aqueous NaOH solution was also loaded into the jar as suspension medium, inducing a synergetic chemical and mechanical peeling of the nanosheets from the powder particles [27]. The suspension was then milled for 24 h in a planetary ball mill (Pulverisette 7 classic line, *Fritsch*, Germany) at 200 rpm, with 90 min pause every 2 h to avoid overheating of neither the equipment nor the suspension. The direction of rotation was also changed in each cycle to ensure homogeneity of the powder exfoliation throughout the milling process. Residual Fe^{3+} from the balls and container was eliminated by adding 100 ml of concentrated HCl (37 %) directly into the collected milled suspension. The product was then washed with DI water using 0.2 μm alumina filters (Anodisc 47, Whatman, Germany) until the filtrated liquid reached neutral pH. The collected solid was re-dispersed in DI water for 30 min in a bath sonicator before centrifugation at 2000 rpm for 30 min (Rotofix 32 A, Hettich, Germany) and two thirds of the supernatant collected with a pipette. The fine suspensions were immediately frozen with liquid nitrogen and then freeze-dried for 48 h to avoid re-agglomeration of the obtained nanosheets during drying (Cryodos-80, Telstar, Terrasa, Spain; Centro de Investigación, Tecnología e Innovación de la Universidad de Sevilla, CITIUS).

The BNNS powder obtained after the hydroxide assisted milling was characterized by X-ray photoelectron spectroscopy (XPS) to corroborate the functionalization of the nanosheets and elucidate the possible

presence of impurities after the exfoliation routines. A SPECS spectrometer coupled with a Phoibos 150 MCD analyzer (SPECS, Germany; XPS service, CITIUS) was used for the measurements with Al Kα radiation ($h\nu$= 1486.6 eV). The survey and region spectra were recorded at 40 and 35 eV pass energy respectively. Ultra-high vacuum (10^{-10} mbar) was ensured inside the analytical chamber. The functionalization of the exfoliated BNNS was also analyzed by thermogravimetric analysis (TGA). The powder sample was heated at 10 °C/min in air from room temperature to 1200 °C with an SDT Q600 V20.9 Build 20 system (TA Instruments, USA; ICMS). Mass fluctuation was recorded over temperature.

The structural integrity and morphology of the BNNS were characterized by Raman spectroscopy and high-resolution transmission electron microscopy (HR-TEM). To that end, a few droplets of BNNS suspension in water were deposited on a glass slide for Raman spectroscopy or on a Cu transmission grid with C coating for HR-TEM inspection after drying. A dispersive microscope Raman Horiba Jobin Yvon LabRam HR800 (ICMS), with a green laser He-Ne (532.1 nm) at 20 mW was used. The microscope used a 100x objective and a confocal pinhole of 100 μm. A few droplets of the sonicated BNNS suspension in water was also deposited on a Cu transmission grid with C coating and were left to dry. TEM and HRTEM images were acquired with a FEI Talos S200 (CITIUS) transmission electron microscope. X-ray energy dispersive (X-EDS) and electron energy loss spectroscopy (EELS) analysis were performed on the nanosheets using a FEI Tecnai field emission gun scanning transmission electron microscope (STEM-FEG), mod. G2F30 at 300 kV, with a 0.2 nm point resolution. EELS was performed using a Gatan imaging filter (GIF), mod. QUAMTUM attached to the microscope. The EELS spectra were recorded from several BNNS, in diffraction mode with with a spectrometer collection angle of 1.02 mrad and an energy resolution of ~ 1 eV.

As the obtained BNNS were OH functionalized according to Lee et al. [27], a suspension stability study was performed in different aqueous suspensions. 2 mg of BNNS were deposited in glass vials and then filled with the different solvents to a 2 cm height from the bottom. After 30 min bath sonication, the vials with the different suspensions were left to settle.

2.1.2. Processing and sintering of the ceramic composites

A 3Y-TZP (TZ-3YB-E, Tosoh Corporation, Japan) powder of 40 nm particle size containing 0.1 – 0.4 vol% Al_2O_3 was used to prepare the composites. Prior to the composite powder preparation, the as-received zirconia powder was annealed at 850 ºC for 30 min to eliminate organic additives.

The exfoliated BNNS were re-dispersed in the solvent forming the most stable dispersions by magnetic stirring. Composite powders with 2.5 vol% BNNS content were prepared by adding the corresponding quantity of 3Y-TZP ceramic powder to the BNNS suspension. The mixtures were further stirred and dried on a hot plate with continuous magnetic stirring. The resulting powders were homogenized in an agate mortar.

The composite powders were spark plasma sintered at 1250, 1300 and 1350 ºC for 5 min operating under vacuum, using heating and cooling ramps of 100 and 50 ºC/min respectively. To prepare disc-shaped samples of 15-mm (SPS model 515 S, Dr. Sinter, Inc., Kanagawa, Japan; CITIUS) or 40-mm diameter (HPD 25 model, FCT Systeme GmH, Germany) and 3 – 4 mm thick, a graphite foil (0.35 mm thick) was placed between the powders and the punches and along the inner wall of the die to ensure their electrical, mechanical, and thermal contact and also for easy removal of the sample. The temperature was monitored by means of an optical pyrometer focused either on the outer wall of the graphite die (for the 15-mm samples) or in a hole drilled in the middle of the graphite die (for the 40-mm samples). A 75 MPa pressure was applied over 700 ºC.

2.2. Microstructural characterization

The bulk density of the composites was measured with the Archimedes' method using distilled water as the immersion medium. The theoretical density was calculated using the rule of mixtures, considering $\rho = 6.05$ g cm^{-3} for the 3Y-TZP and $\rho = 2.10$ g cm^{-3} for the BNNS. The semi-quantitative analysis of the crystallographic phases present in the sintered composites was carried out by X-ray diffraction (XRD, model D8 Advance A25, Bruker Co. Massachusetts, USA; CITIUS). The monoclinic zirconia volume fraction (V_m) was estimated as described by Garvie and Nicholson [28] and Toraya [29], averaging the results from 2–3 XRD patterns performed on different zones of the polished sample surface.

The distribution of the BNNS in the zirconia matrix was characterized by low magnification scanning electron microscopy (SEM, FEI-Teneo, FEI, USA; CITIUS) using backscattered electrons (BSE) for imaging. In order to account for any structural anisotropy of the composites, cross-section (c.s.) and in-plane (i.p.) surfaces, i.e. surfaces parallel and perpendicular to the SPS pressing axis, were analyzed after polishing with diamond paste down to 1 μm. High-resolution SEM was used to examine the fracture surfaces of the composites as well as to characterize their ceramic grain morphology. Polished cross-section surfaces were thermally etched for 20 min in H_2/Ar at 100 ºC below the sintering temperature to reveal the ceramic grain boundaries. To characterize the zirconia ceramic grains, the mean equivalent plane diameter and its corresponding standard deviation were quantified. ImageJ and OriginLab softwares were used to analyze the grain size distributions by measuring more than 300 grains for each material and fitting to a lognormal distribution respectively. The mean linear intercept distance was also estimated using the linear intercept method from SEM micrographs of the composite cross-section (c.s.) surfaces polished down to 0.03 μm using colloidal silica suspension.

(S)TEM characterization was also performed on the composites. For this purpose, planar and cross-section views were prepared following the conventional procedure of mechanical polishing followed by argon ion milling to electron transparency. Microstructural and chemical studies, using high angle annular dark field scanning TEM (HAADF-STEM) images, and nano-probe X-ray energy dispersive (X-EDS) and electron energy loss spectroscopy (EELS) analysis, were performed in several TEM microscopes:

- A FEI Tecnai field emission gun scanning transmission electron microscope (STEM-FEG), mod. G2F30 with an S-Twin objective lens at 300 kV, with a 0.2 nm point resolution, and equipped with a HAADF detector from Fischione with a 0.16 nm point resolution (ICMS) and an EDX detector. EELS was performed using a Gatan imaging filter (GIF), mod. QUAMTUM attached to the microscope. The EELS spectra were recorded in STEM mode using a probe with a size of less than 1 nm, with a spectrometer collection angle of 9.6 mrad. Under these conditions, the energy resolution of the couple microscope/spectrometer system was ~ 1 eV and the lateral resolution around 1 nm.
- A FEI Talos F200X (Universidad de Cádiz). X-EDS elemental maps were obtained by using ChemiSTEM® Technology with four integrated Bruker SDD detectors and processed using Velox® software EELS was performed using a Gatan Continuum spectrometer attached to the Talos F200X microscope.
- A double aberration-corrected FEI Titan3 Themis 60–300 microscope (Universidad de Cádiz) working at 200 kV. X-EDS maps were obtained by using ChemiSTEM® Technology with four integrated Bruker SDD detectors and processed using Velox® software. EELS spectra were recorded with a GIF Gatan Quantum 966ERS.

After experimental acquisition, images and X-EDS and EELS spectra were processed using the Velox and Gatan Digital Micrograph software, respectively.

2.3. Mechanical characterization

To evaluate the hardness of the composites, at least 10 Vickers indentations were performed on the cross-sections (c.s.) of the materials polished down to 1 μm with diamond paste. A load of 98 N (P = 10 kgf) was applied with a Wilson indenter (Wilson VH 1150, Buehler) for 10 s on the mirror-like surfaces and an optical microscope was used to measure the indent diagonals lengths (d_V in mm). The hardness was then calculated with the following equation:

$$H_V = 1.854\left(\frac{P}{d_V^2}\right) \quad (1)$$

The Young's modulus (E) was calculated by the impulse excitation technique with a Grindosonic MK6-A (GrindoSonic BV, Belgium) on rectangular bars of 3 mm × 3.8 mm× 25 mm (b x w x L) machined from the 40-mm diameter SPSed samples. The specimens were placed on low-density polymer supports and the microphone on the opposite side of the excited surface. This equipment displays the natural frequencies which allow E to be determined as specified in the E1876–01 ASTM standard [30]. For each material, 10 bars were tested to estimate the averaged elastic modulus and its dispersion. Shear modulus and Poisson's ratio could not be measured due to the limited dimensions of the specimens; hence, the Poisson's ratio was supposed to be 0.3.

Fracture toughness (K_{IC}) and crack growth resistance curves (R-curves) were evaluated following the single-edge V-notched beam (SEVNB) method. In order to apply the international standards, rectangular bars of 3 mm × 3.8 mm× 25 mm (b x w x L) were machined from the 40-mm diameter SPSed discs. The straight-through-thickness V-notch was performed in the middle of the tensile side of the specimens, parallel to the SPS pressing axis (Fig. 1). The notch-length-to-width ratio ($\alpha = a_0/w$), being a_0 the total notch length (Fig. 1), was 0.3 for the K_{IC} measurements and 0.5 for the R-curve analyses. A first pre-notch was performed with a 0.3 mm thick diamond-coated saw and the last 200 μm length was machined by ultrashort pulsed laser ablation (UPLA) to obtain a very thin notch root, as previously validated for submicron and nanograined ceramics [31–33].

The ablation was induced by focusing near infrared ultrashort laser pulses (795 nm wavelength, 60 fs duration and 5 kHz repetition rate), delivered by a Ti:Sapphire oscillator (Mai Tai, Spectra Physics, USA) combined with a regenerative amplifier (Spitfire Ace, Spectra Physics) based on the chirped pulsed amplification technique. To perform the notches, the samples were placed on a XYZ motorized stage and moved along one of the horizontal axes. An achromatic doublet lens of 50 mm focal length was used to focus the laser pulses and a multiple pass strategy was followed, requiring 36 passes of 36 μJ pulses at a scanning speed of 400 μm/s, to attain the required notch depth.

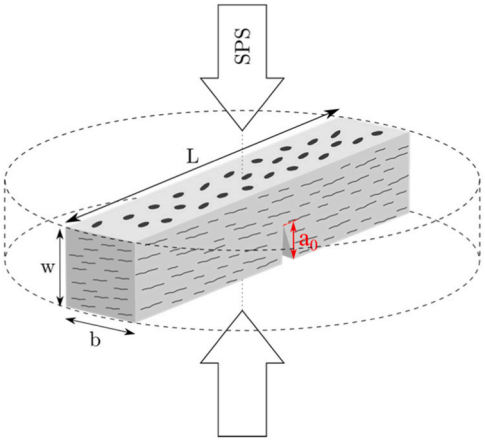

Fig. 1. Scheme of the single-edge V-notched beam indicating the notch orientation in relation with the sintered disc. The white arrows indicate the SPS pressing axis.

K_{IC} was measured in a four-point bending configuration, with support-outer and -inner spans of $S_1 = 21$ mm and $S_2 = 10$ mm, using an INSTRON 8500 machine (Norwood, USA). The specimens were loaded in air at a constant displacement-controlled speed of 0.5 mm/min. K_{IC} was calculated as the stress intensity factor (K_I) for the maximal applied load, P_{max} [34]:

$$K_I = Y\left[\frac{P(S_1 - S_2)10^{-6}}{bw^{3/2}}\frac{3\sqrt{\alpha}}{2(1-\alpha)^{3/2}}\right] \quad (2)$$

where Y is a geometrical factor, P is the load, S_1 and S_2 stand for the support-outer and -inner spans respectively, and w and b are the width and depth of the samples respectively. Y is a function of α (a_0/w) and depends on the configuration of the bending test. For a four-point bending configuration, Y is calculated as [34]:

$$Y = 1.9887 - 1.326\alpha - \frac{\alpha(1-\alpha)(3.49 - 0.68\alpha + 1.35\alpha^2)}{(1+\alpha)^2} \quad (3)$$

At least three measurements were performed on each material and the dispersion from the mean value was considered as the demi-dispersion of the individual K_{IC} values. The total notch length (a_0)was estimated from three measurements taken on the fracture surfaces of the specimens after the bending tests by means of an optical microscope, as specified in ASTM C1421-10 standard [34].

Resistance to stable crack growth (R-curve) of the materials was estimated from the compliance method [35], which has been recently validated for similar composites [13], on SEVNB by three-point bending tests. Three 8 mm diameter alumina cylinders were used as contact points with a support span of 20 mm (S_1). The deflection (δ) was recorded by means of a linear variation displacement transducer (LVDT) placed right next to the notch aperture. The tests were conducted in air at a constant LVDT displacement speed of 10 μm/min and unloaded before complete failure at 100 μm/min to ensure no further crack propagation.

To evaluate the effect of slow crack growth in the composites, the R-curve was also evaluated on a specimen impregnated in extra virgin olive oil. Olive oil was chosen among other oils because of its lower water content. The impregnation protocol was stablished following the international standard for density measurements through liquid immersion (ASTM C373–18 [36]) and the methodology presented by Chevalier et al. [37]. To remove moisture and isolate the crack path from the air humidity, the specimen was placed in a desiccator under a vacuum of 10^{-2} mbar for 2.5 h, after properly drying it in stove at 105 °C (more than 2 h). The immersion liquid was also placed inside the desiccator to minimize air in the oil. Later, the specimen was immersed in the olive oil maintaining the vacuum for another 2 h. Normal pressure was recovered just before the testing, to ensure no contact with the environmental humidity. The oil on the surface was removed rapidly before placing the specimen on the testing jig to avoid sliding of the LVDT.

From each instantaneous force and deflection data pair (P_n and δ_n) – being n the position of the data in the succession –, the instantaneous crack-growth resistance ($K_{IR,n}$) and crack length (a_n) were estimated using the compliance approach to represent the R-curve [35]. $K_{IR,n}$ is calculated using Eq. (2), with $S_2 = 0$ mm, and P each instantaneous load value. In the case of the three-point flexure configuration with $5 \leq w/S_1 \leq 10$, the geometry factor, Y, is defined as:

$$Y = A_0 - A_1\alpha + A_2\alpha^2 + A_3\alpha^3 + A_4\alpha^4 + A_5\alpha^5 \quad (4)$$

A_i being polynomial coefficients that depend on the w/S_1 ratio [34].

The real crack length at the end of the test, a_f, was measured on the surface of the specimens (polished down to 1 μm before notching) with an optical microscope to account for any difference with the calculated final crack length ($a_{n,max}$). Less than 2 % difference between the

measured crack length and that estimated by the compliance approach was observed, confirming the validity of this method for R-curve measurement in these materials. The crack length values obtained by the compliance approach (a_n) were then proportionally corrected by successively adding that difference to every point as follows:

$$a_{n,cor} = a_n + n\left(\frac{a_f - a_{n,\max}}{n_{\max}}\right) \quad (5)$$

For each material, the R-curve parameters (K_{I0} and $\Delta K_{I,th}$) were averaged from at least three measured curves and their dispersion calculated.

For all the specimens, the total notch length (a_0) was estimated as specified in the K_{IC} measurements. The fracture surfaces and the crack paths before failure were also analyzed by SEM (Zeiss SUPRA VP55, Switzerland) to investigate the possible toughening mechanisms.

The stress-induced transformed monoclinic fraction over less than 2 μm depth below the fracture surface was estimated by grazing-incidence XRD (GIXRD). A Weibull mirror was coupled to a fix 0.2° slit in the incident beam of the diffractometer. The scans were acquired on the crack plane after fracture, from 27° to 33° with a step size of 0.02° and a time per step of 30 s. The monoclinic volume fraction (V_m) was calculated from the XRD patterns as described in section §2.2.

3. Results and discussion

3.1. Analysis of the BNNS exfoliated by hydroxide-assisted planetary ball milling

A thorough study of the particles obtained after the hydroxide assisted ball milling of h-BN proved the successful exfoliation of BN nanosheets (see section S1 of the Supplementary Information), presenting lateral sizes ranging from 50 nm to ~ 3 μm (Fig. S1 of the Supplementary Information). Mostly thin BNNS with 9 – 15 h-BN layers were obtained although thicker particles of up to 40 – 60 h-BN were also observed (Fig. S1). The nanostructure structural integrity after the high energy process was confirmed by Raman and electron energy loss spectroscopies (Fig. S2), as only the characteristic peaks of hexagonal BN were detected. Furthermore, no impurities were detected on the BNNS powder by XPS, which revealed the partial surface hydroxylation of the nanostructures (section S1). This functionalization was further corroborated by thermogravimetric analysis (Fig. S2).

Pristine h-BN is known to exhibit superhydrophobicity [38], but the introduction of -OH functional groups may interact with water molecules, promoting stable suspension in aqueous solvents [27,38]. Stable suspensions are a key factor for the preparation of composite materials with 2D nanostructures. Ensuring a well-dispersed 2D-BN during its mixture with the ceramic powder in a liquid medium fosters a better dispersion of the filler throughout the matrix after sintering, avoiding agglomeration that would deteriorate the composite properties. Since the BNNS analysis revealed the partial hydroxylation of the nanosheets, the suspension stability of the BNNS in DI water at various pH was investigated to determine the optimal suspension medium (see section S2 of the Supplementary Information). Stable suspensions were obtained in the aqueous solutions at various pH ranging from 5 to 11, even after one-week settlement. So, to ensure the most environmentally friendly procedure, DI water (pH ~ 7) was selected as the dispersion medium for the composite powder preparation.

3.2. Influence of the sintering temperature on the composite microstructure

3.2.1. Integrity and distribution of the BNNS

Low-magnification BSE-SEM images of the polished cross-section and in-plane surfaces (c.s. and i.p.) surfaces of the composite sintered at 1250 ºC are presented in Fig. 2a and b, respectively. According to the distinct average atomic number, the BNNS and the 3Y-TZP appear as dark and light phases, respectively. The BNNS were homogeneously distributed throughout the ceramic matrix, presenting a reduced number of agglomerates. Although the BNNS were randomly distributed on the i.p. surface (Fig. 2b), a preferential alignment of the nanosheets was observed on the c.s. (Fig. 2b), where the BNNS main *ab* plane laid perpendicular to the SPS pressing axis, in agreement with previous studies on similar 3Y-TZP/BNNS composites [24]. The sintering temperature did not affect the 2D character of the nanosheets nor their distribution, since all the composites presented analogous microstructural anisotropy (not shown).

The fracture surface of the composites (Fig. 3a – d) was observed by SEM, where the BNNS are easily recognized as the darkest phase due to the Z contrast. These micrographs are representative of all three composites, as no significant differences were observed among the materials SPSed at the different temperatures (1250, 1300 or 1350 °C). Large BNNS (~ 2 – 4 μm) were found in small groups between the ceramic grains (Fig. 3a and b). The squared area in Fig. 3a reveals that the thicker BNNS are formed by several individual BNNS, where the top nanosheet shows some kinks. Intergranular individual nanosheets were also observed (marked by a red arrow in Fig. 3a) dispersed throughout the 3Y-TZP matrix. These nanostructures are very rigid, showing flat surfaces that do not adapt to the shape of the ceramic grains. The powder homogenization and sintering processes did not affect the BNNS shape, since BNNS with straight angles were witnessed (Fig. 3b) as the ones revealed in section S1 of the Supplementary Information. Occasionally, folded nanosheets with sharp angles were found (circled area in Fig. 3a) confirming the BNNS stiffness. The rigid nature of the BN nanosheets strongly restrained the ceramic grain growth in the direction of the nanostructure, as revealed by the flat ceramic grains found around and below some of the BNNS stackings (Fig. 3c and d). The dark translucent areas on top of these flat grains reveal thin nanostructures that seemed to be stacked and remained attached to the ceramic matrix after fracture.

Inspection of the 3Y-TZP/BNNS composites by HAADF-STEM, also

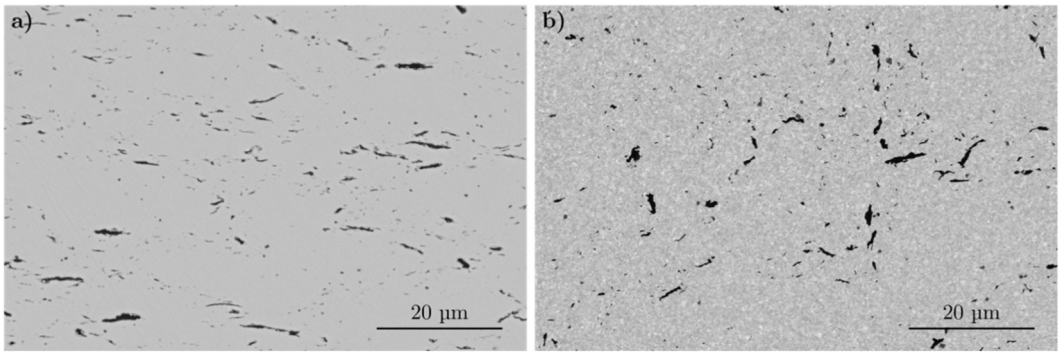

Fig. 2. – BSE-SEM micrographs of the Z-2.5B-1250 composite on the polished a) cross-section and b) in-plane surfaces.

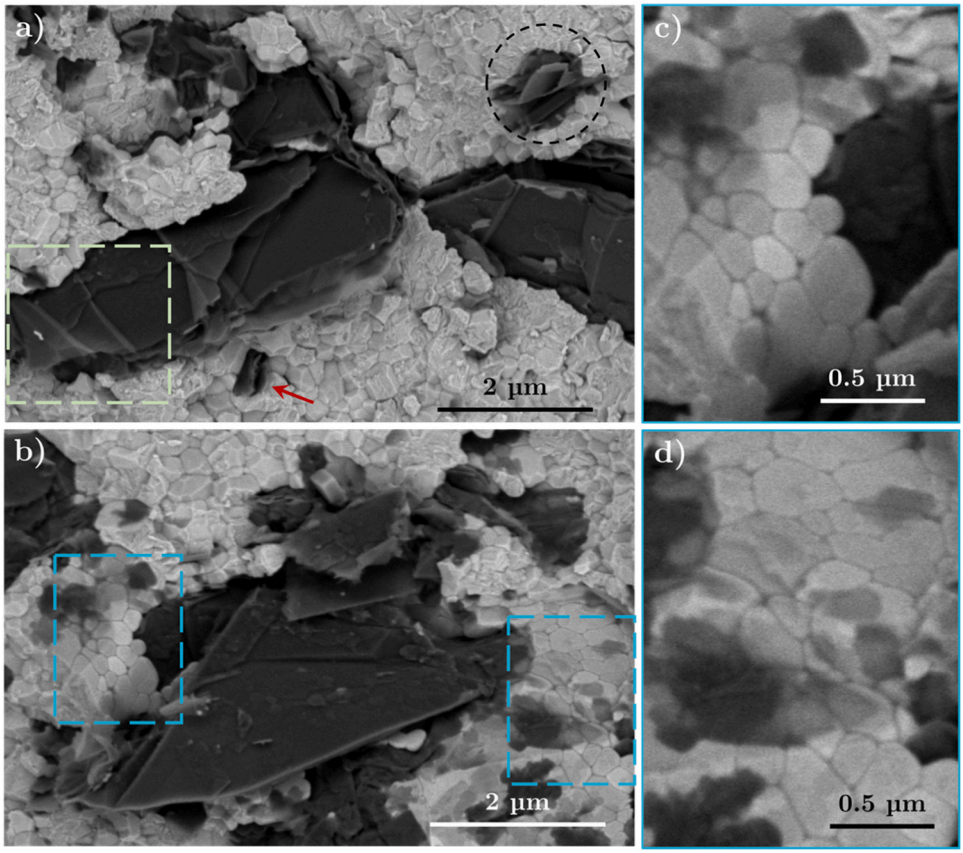

Fig. 3. SEM micrographs of the Z-2.5B-1250 composite fracture surface. a) A flat intergranular individual BN nanosheet is marked by an arrow, whereas thicker platelets are composed of thinner ones, as deduced from the kinked top layer nanosheet in the squared area. Most nanosheets are flat, but folded nanosheets with sharp angles (circled) are also found. b) Flat ceramic grain areas are observed in the squared areas and amplified in c) and d).

called Z-contrast image because the signal intensity is proportional to $Z^{3/2}t$ (where Z is the atomic number and t is sample thickness), (Fig. 4a) revealed the presence of thinner and smaller BNNS (from 70 to 500 nm in diameter) than the ones detected by SEM, presenting no preferential orientation at this scale. As illustrated in Fig. 4a, the nanosheets were equally found with their c axis parallel (circled BNNS) or perpendicular (marked with arrows) to the electron beam. In Fig. 4b, a representative HRTEM image of the BNNS area is shown, where the presence of lattice fringes evidences the integrity of the BNNS crystallinity in the composite after sintering. The first three rings in the digital diffraction pattern (DDP) obtained from this image (see insert) correspond to interplanar spacing values of 3.38 Å, 2.17 Å and 1.86 Å, that can be respectively assigned to (002), (100) and (10−2) family plane of the h-BN phase. The observed rings corroborated that nanosheets with different orientations are present in the same area [1,26,39]. This observation suggests that small BNNS, which have lower contact area, are prone to remain randomly oriented despite the 75 MPa uniaxial pressure during sintering with SPS. Similar conclusions were derived by López-Pernía et al. [40], who obtained orthotropic graphene nanoplatelets (GNP)/3Y-TZP composites with exfoliated GNP of reduced lateral dimensions. The planar lattice of the BNNS is shown in HRTEM (image Fig. 4c), further confirming its 6-fold symmetry. The diffraction pattern observed in the inset of Fig. 4c revealed the stacking of several parallel nanosheets slightly rotated relative to each other. Since the Raman analysis on the as-exfoliated BNNS pointed to the detection of mainly single layer h-BN, it seems that 2D-BN may have been restacked during suspension and deposition.

X-EDS elemental maps were acquired over an area containing several BN nanosheets (Fig. 5). The B and N signals coming from the nanosheets on the HAADF-STEM image were well differentiated from Zr, O and Y signals of the zirconia grains, inferring that the nanosheets were pure, with no impurities in them. Furthermore, the absence of oxygen over the regions corresponding to the BNNS points to the reduction of the OH-BNNS during SPS sintering. Higher yttrium contents were detected at the ceramic grain boundaries, inferring segregation from the ceramic grains. The Y enrichment of the grain boundaries is common in Y-TZP materials [41].

Besides the elemental composition of the nanosheets inside the composite confirmed by X-EDS, evaluation of the electronic structure would inform of the crystallographic phases present in the nanostructure after the sintering process. The EELS spectra in Fig. 5 were acquired on regions marked as I and II, due to the apparently different disposition of the BNNS, planar or transversal to the electron beam. Both spectra show the typical B K-edge and N K-edge EELS for h-BN, confirming the exclusive presence of the hexagonal phase. The relative intensity of the π^* edge (~ 192 eV) to σ^* edge (~ 199 eV) in the B K-edge EELS provide information about the orientation of h-BN, as the π orbitals lie parallel to the c-axis. When the π^* orbital (i.e. the c axis) of the hexagonal structure is parallel to the electron beam, the intensity of the π^* edge is lower than that of the σ^* peak. Contrarily, if the c axis in h-BN is perpendicular to the electron beam, the π^* edge intensity from the B spectrum is greater than the corresponding σ^* edge [42]. Therefore, the low π^*/σ^* edge intensity ratio observed in the EELS spectrum from region I indicates that the nanosheet was placed with its c-axis parallel to the electron beam, whereas in region II the BNNS was sideways as corroborated by the high intensity of the π^* edge relative to the σ^* edge. Therefore, it can be concluded that the BNNS in the composite retained the highly oriented hexagonal structure even after SPS.

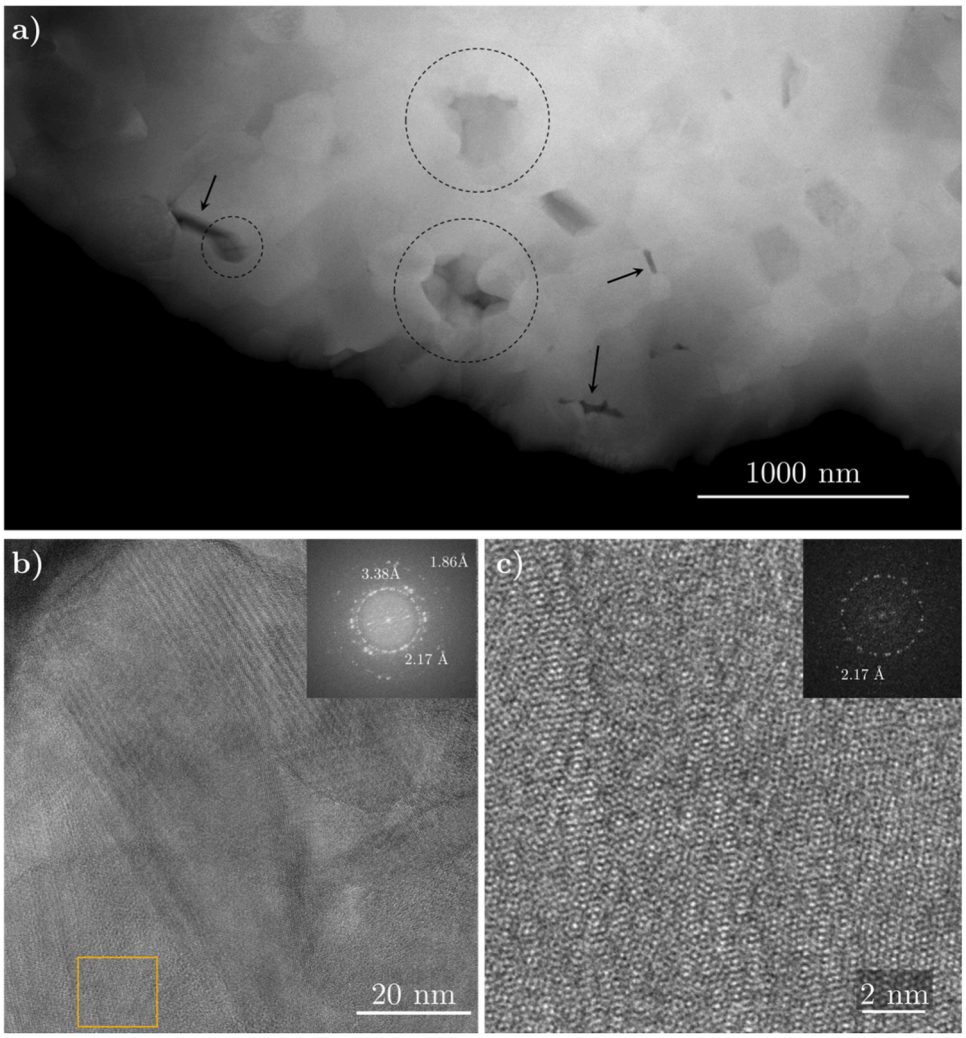

Fig. 4. – a) HAADF-STEM image of the Z-2.5B-1250 composite. Some BNNS are marked by arrows (BNNS parallel to the electron beam) or circled (BNNS perpendicular to the electron beam. b) HRTEM image of several stacked BN nanosheets in the composite. c) HRTEM image of the planar lattice structure of the BNNS region squared in b). The insets in b) and c) include the digital diffraction pattern (DDP) of the images.

3.2.2. Microstructural evolution of the zirconia matrix

No significant effect of the BNNS incorporation on the relative density of the composites was observed, and complete densification (> 99 %) was attained in all the materials (Table 1). This is in agreement with previous published results for different ceramics with BNNS as fillers, in which just slight decreases in density were observed when increasing the BNNS content [2–6]. No effect of the sintering temperature on the densification of the materials was observed either.

The reduced tetragonal zirconia ($ZrO_{1.95}$, JCPDS 01–081-1544) was the main crystallographic phase revealed by the XRD patterns of the sintered composites (Fig. S4 of the Supplementary Information). A widening on the left side of the peak with the highest intensity ($\theta \sim 30.2^{\circ}$) indicates that there is a small contribution of the zirconia and yttria solid solution with cubic structure, $Zr_{0.80}Y_{0.20}O_{1.9}$ (JCPDS 01–082-1246).

The reported literature on the effect of h-BN nanostructures on the ceramic microstructure development has not reached conclusive results up to now. The existence of many factors that can influence the microstructure and that are usually different in the published works, i.e. the sintering technique or the type, size and purity of the BN nanostructure, makes it extraordinarily difficult to obtain general conclusions about the effect of BNNS on the microstructure.

In this work, the introduction of the partly hydroxylated BNNS nanosheets to the zirconia matrix enhances grain growth (see section S3b of the Supplementary Information), enlarging the ceramic grains (0.32 vs. 0.21 μm, Table 1) and broadening their distribution (0.24 vs. 0.12 μm, Table 1) when compared to the monolithic 3Y-TZP sintered at 1250 °C. This is more remarkable in the composites sintered at higher temperatures, in which grains as large as 1.1 μm were found in the Z-2.5B-1350 composite. The grain size distributions and micrographs of the etched surfaces can be found in Fig. S5 of the Supplementary Information. It should be noted that the microstructures in this figure appear slightly overetched, so lower etching temperatures/times should be used in future works.

Contrarily, a refinement of the microstructure has been reported for AlN [3,4], Al_2O_3 [11] or Si_3N_4 [2,20] composites with BNNS, independently of the sintering technique - hot pressing [3,11], conventional sintering [4], or SPS [2,20] - or the size of the BN nanostructure. A pinning effect has been proposed as responsible of the downward trend of AlN [3,4] or Si_3N_4 [20] grain size with the increase of the BNNS content, as the BN nanosheets present at the grain boundaries would inhibit the grain growth by obstructing boundary movement. This grain boundary pinning was also pointed out as the main cause to restrain abnormal grain growth in Al_2O_3 ceramics [11].

Regarding 3Y-TZP composites, studies about the influence of BN nanostructures on the ceramic microstructure development are very scarce. Xu et al. [43] reported the absence of a clear trend of the grain size evolution with the BN nanotubes (BNNT) content. For composites

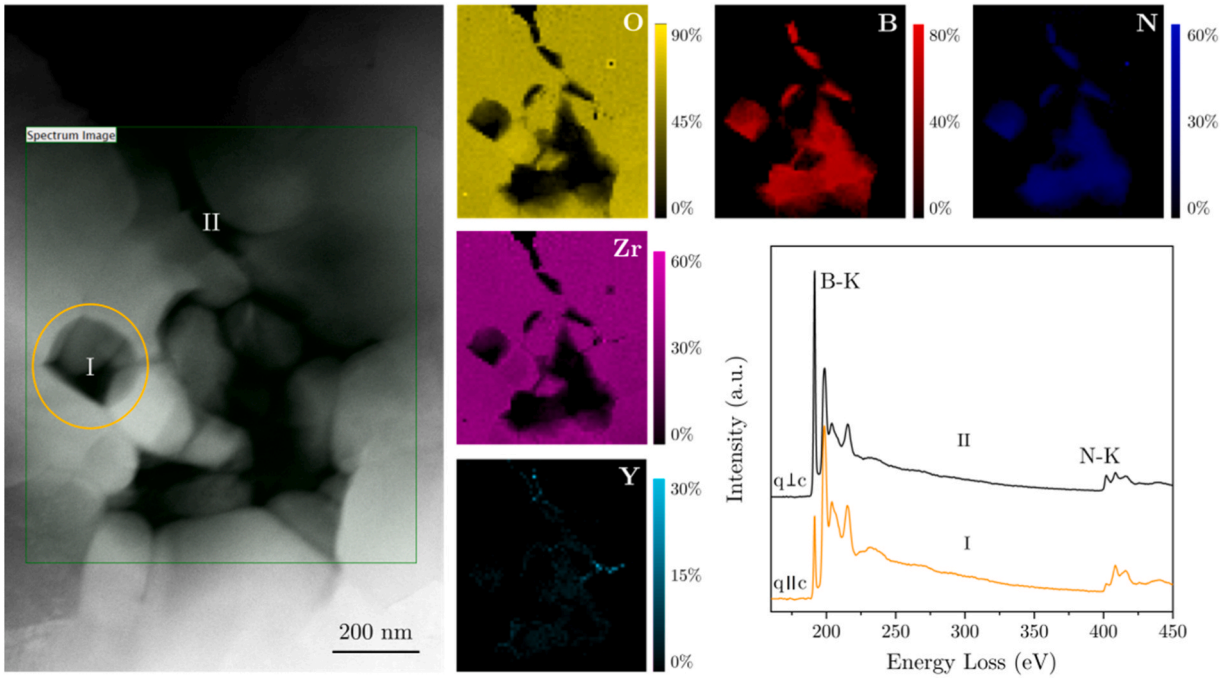

Fig. 5. Elemental maps obtained from the square region of the HAADF-STEM image of the Z-2.5B-1250 composite showing the contributions from Zr, O, Y, B and N, and EELS spectra of the planar (I) and transversal (II) BN observed on the image.

Table 1
Relative density, zirconia mean grain size and standard deviation of the studied composites.

Sample	Sintering temperature (°C)	Relative density (%)	Mean grain size (μm)	Standard deviation (μm)
3Y-TZP	1250	100	0.21	0.12
Z-2.5B-1250	1250	100	0.32	0.24
Z-2.5B-1300	1300	99	0.37	0.25
Z-2.5B-1350	1350	99	0.47	0.25

up to 1 wt% BNNT, a decrease in the grain size was observed, however, it increased in the composite with 2 wt% BNNT. On the contrary, a significant grain size increase after the addition of BNNT contents up to 5 wt% was reported by Tatarko et al. [21]. These authors detected by HR-TEM the presence of a glassy phase at the multiple grain junctions of composites with 0.5 and 1 wt%, and even at some of the grain boundaries of composites with 2.5 and 5 wt%. No vitreous phase was observed either at the grain boundaries or in the multi-grain junctions of monolithic zirconia. They suggested that this behavior may be related to the presence of residual metal catalysts inside the BNNT (Fe, Si, Mg, Al). The authors assumed that these catalysts were in the form of metal oxides and would act as additives that changed the sintering behavior from solid-phase to liquid-phase sintering [44,45], increasing densification and grain growth in the ceramic [21]. However, the composition of the glassy phase was not analyzed in the study.

The formation of a liquid phase during sintering has been also suggested by Kim et al. [46] for ZTA composites with BNNT contents up to 0.5 wt%, in which the BNNT hardly suppressed the grain growth. In this case, they related the vitreous phase to the presence of chemically uncombined elemental boron in the as-received BNNT, which forms B_2O_3 in the step of binder burnout during the powder processing and transforms into liquid phase at temperatures over 450 °C during sintering. A densification enhancement related to liquid-phase sintering has also been described in TiB_2/h-BN [47] and Si_3N_4/BNNS [2] composites. However, in these studies the additives that would have caused the liquid phase would not exclusively come from the h-BN fillers. Nguyen et al. [47] described a B_2O_3-TiO_2 liquid phase that would come from an oxide layer naturally present on the initial TiB_2 powder [48]. Furthermore, the addition of h-BN particles, whose surface can be oxidized at room temperature, would provide a larger amount of B_2O_3. Tatarková et al. [2] identified an amorphous phase mainly located at the ceramic triple junctions by HR-TEM. A thin intergranular amorphous film was also found at some ceramic grain boundaries, as commonly observed in Si_3N_4 materials with sintering additives [49]. Even though the composition of the amorphous phase was not established in the study, the authors concluded that it was formed by the sintering additives (Y_2O_3 + Al_2O_3) during sintering.

In the present study, glassy phase pockets at some triple junctions of the ceramic grains (Fig. S6 of the Supplementary Information) were observed by HAADF-STEM, which seemed to increase in size or number with growing sintering temperature. High-resolution TEM imaging (Fig. 6) confirmed the amorphous character of this phase, which is mainly constituted of Al, Si and Y, as revealed by the X-EDS elemental maps depicted in Fig. 6. We have not detected the presence of B_2O_3 phase neither by EDX nor by EELS spectroscopies, contrarily to what was suggested by previous authors [46,47]. Despite the absence of B in the glassy phase, the formation of volatile or reactive intermediate B-containing compounds cannot be discarded. A thin intergranular amorphous film with ~ 2 nm thickness and similar composition was also found at some of the ceramic grain boundaries extending from the pockets at the triple junctions (Fig. 6). Several studies have reported the formation of a vitreous phase in SiO_2 or SiO_2-Al_2O_3 doped 3Y-TZP ceramics [41,50,51]. In the present study, a significant yttrium segregation towards most of the grain boundaries was evidenced (Fig. 6), which would have enriched the glassy phase in this element. The Al_2O_3 content in the initial 3Y-TZP powder could have added to the Al and Si impurities in the BNNS (detected by X-EDS, see section S1). Al and Si were present in the h-BN starting powder but the milling balls and container could also have added some metallic impurities. Most probably a certain threshold of impurities content in the form of metal oxides that would act as additives was exceeded, modifying the sintering behavior from

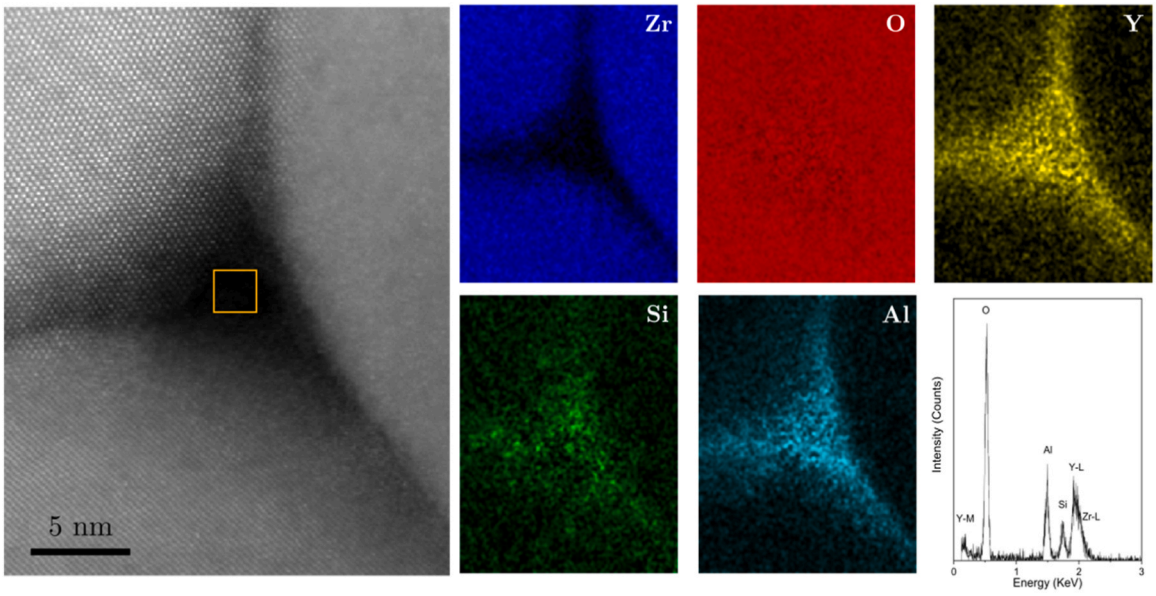

Fig. 6. HRTEM images and X-EDS elemental mappings of a pocket in the triple junction of ceramic grains on the Z-2.5B-1250 composite and the corresponding X-EDS spectra from the squared region.

solid-phase to liquid-phase sintering. The effect of the glassy phase on the grain growth can be inferred from Fig. S6a of the Supplementary Information. Larger grains were observed on the right side of the image where some pockets were located, whereas finer grains were found in the region with no pockets (left side in Fig. S6a of the Supplementary Information). The wider grain size distributions obtained with increasing sintering temperature could also be related to the liquid phase sintering. At higher temperatures, a larger amount of the liquid phase would have formed, as inferred from the increased number of pockets in the Z-2.5B-1350 composite compared to the Z-2.5B-1250 (Fig. S6c and a of the Supplementary Information, respectively), or from the bigger size of such pockets in the Z-2.5B-1300 material (Fig. S6b of the Supplementary Information). Thus, the presence of a small amount of liquid phase could have produced an enhanced grain growth by providing a path for rapid material transfer [21].

3.3. Assessment of the 3Y-TZP/BNNS interfaces

The analysis of the interfaces between the filler and the ceramic matrix is a key factor in understanding the properties of a composite material. Previous works in oxide ceramics incorporating graphene oxide (GO) reported the formation of Zr-O-C chemical bonding at the interface, which was attributed to the in-situ reduction of GO during sintering [23,25]. The formation of such intermediate phases was suggested as a strong bonding between the nanofillers and the matrix, related with the toughening observed in rGO/ceramic composites [12, 19,23,25]. An oxycarbide interphase was also spotted in zirconia composites when incorporating few-layer graphene (FLG) with low oxygen content compared to rGO [52]. Thus, even the presence of very little oxygen quantities in the nanosheets may promote the chemical bonding at the nanosheet/ceramic interface. Previous works on 3Y-TZP composites reinforced with BN nanotubes (BNNT) detected the presence of interphases between the BNNT and the matrix [21,43], in contrast with the clean interfaces reported in BNNS/Si_3N_4 composites [2]. Since the BNNS incorporated to the 3Y-TZP in the present study were partly hydroxylated, a systematic assessment of the BNNS/zirconia interface is necessary to determine the interaction among both phases and to which extent the sintering temperature may have influenced the interphase formation.

The zirconia/BNNS interface was investigated by HR-TEM in all the sintered composites. Abrupt interfaces were mostly observed (Fig. 7a and b), regardless of the sintering temperature used to consolidate the material. A transversal BN nanosheet – with its c-axis perpendicular to the electron beam – placed between two zirconia grains is shown in Fig. 7a. The HR-TEM at higher magnifications (Fig. 7b) reveals an abrupt transition from the zirconia grain to the BNNS, which conserves the interplanar spacing of h-BN (~ 3.4 Å), in agreement with the observations made by Tatarková et al. [2] on BNNS reinforced Si_3N_4. Dislocations may also be observed in these micrographs revealing some defects in the structure that were not previously detected. However, an amorphous layer was occasionally found separating the BNNS from the matrix. Fig. 7c shows a representative image of such interphase of ~ 9 nm thickness between a BN nanosheet and the 3Y-TZP grain. As previously mentioned, amorphous interphases were also found on 3Y-TZP/BNNT composites, although a systematic study evidencing its composition was missing [21,43]. In the present work, EELS spectroscopy was performed on the amorphous phase (Fig. 7d) revealing that this layer is composed of amorphous carbon. This C rich phase could come from contamination occurring during the composite preparation, confirming the absence of any 3Y-TZP/BNNS intermediate phase.

Although no apparent BN/zirconia interphases were detected, some of the nanosheets were meticulously evaluated by X-EDS and EELS to determine the reduction degree of the BNNS inside the composite. Compositional mapping of the central nanosheets observed in the HAADF-STEM image (Fig. 8) corroborates the distinct composition of the nanosheet and the matrix. Representation of the content profile for each element along the BNNS thickness in the selected area of the RGB image reveals otherwise. Whereas abrupt transitions occur between the B/N and Zr/Y signals at the edges of the nanosheet (~ 0.015 and ~ 0.066 μm), some oxygen was perceived on ~ 0.005 μm thick borders of the BNNS. EELS spectra were also acquired on the center and on the interphase of the top-most BNNS of the image, revealing that the O K-edge was only detected at the interfacial surface. It should be noted that several nanosheets were inspected and oxygen detection was only found in very limited cases. Hence, it is concluded that most BNNS have properly reduced during the SPS process, and that such reduction does not promote intermediate phases between the BNNS and zirconia disregarding the sintering temperature.

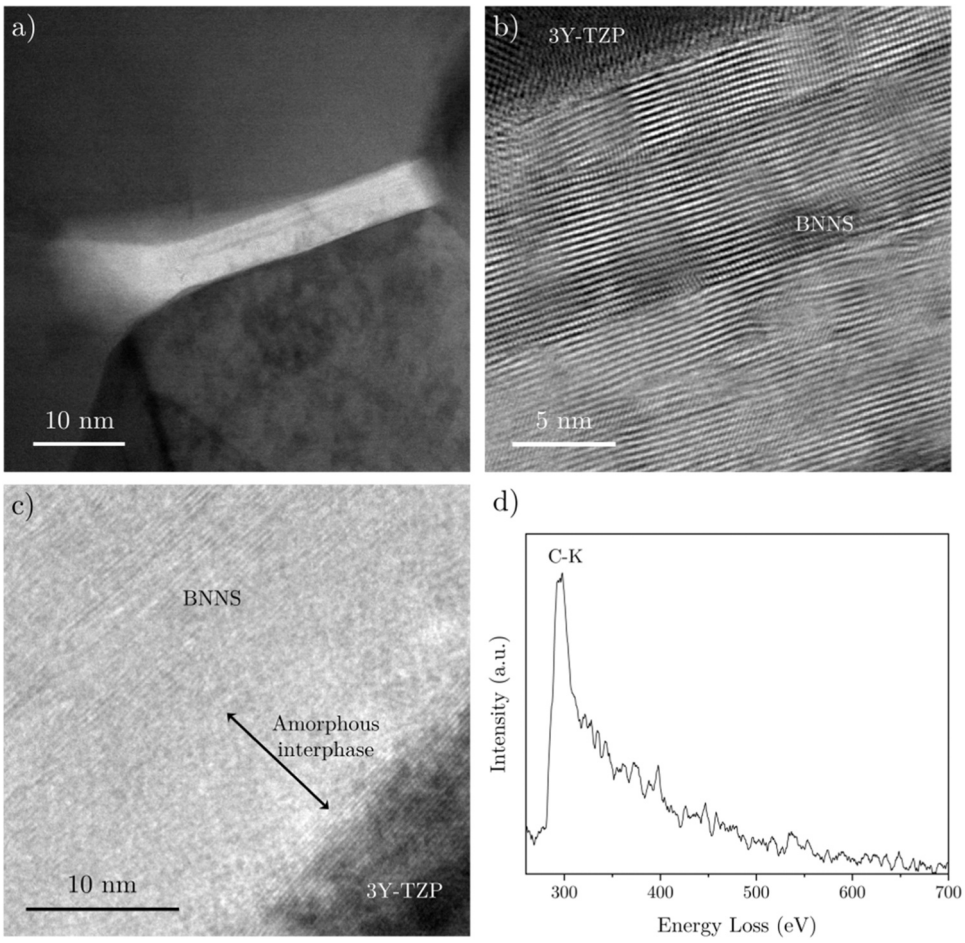

Fig. 7. a) HRTEM images of a representative BNNS in the 3YTZP matrix with abrupt interphases, shown at higher magnification in b). Representative c) HRTEM image and d) EELS spectrum of the amorphous BNNS/3YTZP interfaces.

3.4. Evaluation of the crack growth resistance

The mechanical properties were evaluated on the composite presenting the finest microstructure, i.e. SPSed at 1250 ºC, since the BNNS/3Y-TZP interfaces were clear disregarding the sintering temperature . The Z-2.5B-1250 was proven to be scalable, as fully dense, larger specimens were obtained with similar grain size to that observed on the smaller SPSed sample (see section S4 of the Supplementary Information).

The introduction of the BN nanostructures to the 3Y-TZP matrix slightly decreased the Vickers hardness and Young's modulus of the reference zirconia (Table 2), but it did not impact the fracture toughness ($K_{IC} \approx 4.2$ MPa·m$^{1/2}$, Table 2), as discussed in section S5 of the Supplementary Information.

The resulting R-curves calculated by the compliance method for both materials are illustrated in Fig. 9. To the best of our knowledge, this is the first time that R-curves are reported for BNNS reinforced ceramic composites. Table 2 summarizes the R-curve parameters for each material averaged from at least three tests. The monolithic zirconia presented an almost flat R-curve, increasing the crack growth resistance from a crack-tip toughness (K_{I0}) of $\sim$ 3.3 MPa·m$^{1/2}$ to a plateau toughness ($K_{IR,plateau}$) of $\sim$ 3.6 MPa·m$^{1/2}$ (Table 2). Similar values were already measured for 3Y-TZP materials of comparable grain sizes [13, 53].

The introduction of BNNS rises the R-curve of the composite above that of zirconia and drastically modifies the composite performance regarding crack growth. The Z-2.5B-1250 crack-tip toughness increases by about 30 % relative to that of the reference ceramic. A rising R-curve is observed with an increasing crack growth resistance of 1.1 MPa·m$^{1/2}$, from $K_{I0} = 4.2$ MPa·m$^{1/2}$ to the plateau. The larger K_{IR} increment in the composite occurs at short crack lengths (before 0.1 mm extension), which indicates that the toughening mechanisms are mainly activated at the beginning of the crack propagation. To adequately evaluate the influence of the BNNS incorporation to the 3Y-TZP matrix, the material intrinsic toughness (K_{I0}) and the possible extrinsic toughening mechanisms are discussed in the following sections.

3.4.1. Analysis of the intrinsic toughening

The addition of BNNS increases the composite K_{I0} by about 30 % compared to the monolithic zirconia, resulting in a tougher material. Although this could be attributed to the difference in grain size (see section S4 in suppl. info) [53], the composite and its zirconia counterpart attained similar K_{IC} values during unstable crack propagation (Table 2). This finding suggests that the variation in grain size was irrelevant with respect to the material toughness. Thus, the K_{I0} increase in the Z-2.5B-1250 composite cannot be related to toughening by grain growth, and it is a direct effect of the BNNS incorporation.

The fact that K_{I0} differs from K_{IC} in the 3Y-TZP sample is a clear sign of stress-assisted corrosion by water molecules of the 3Y-TZP, i.e. slow crack growth (SCG). SCG is only noticeable when the ambient moisture has enough time to penetrate to the crack tip, for instance in stable crack propagation tests rather than on the more rapid K_{IC} measurements as the load in the latter was applied at higher rates than in the former ones (i.e. 0.5 mm/min vs. 10 μm/min). Indeed, the highest measured crack tip toughness of the Z-2.5B-1250 composite exactly matched the fracture toughness of the materials ($K_{I0} = K_{IC} = 4.2$ MPa·m$^{1/2}$ for Z-2.5B-1250,

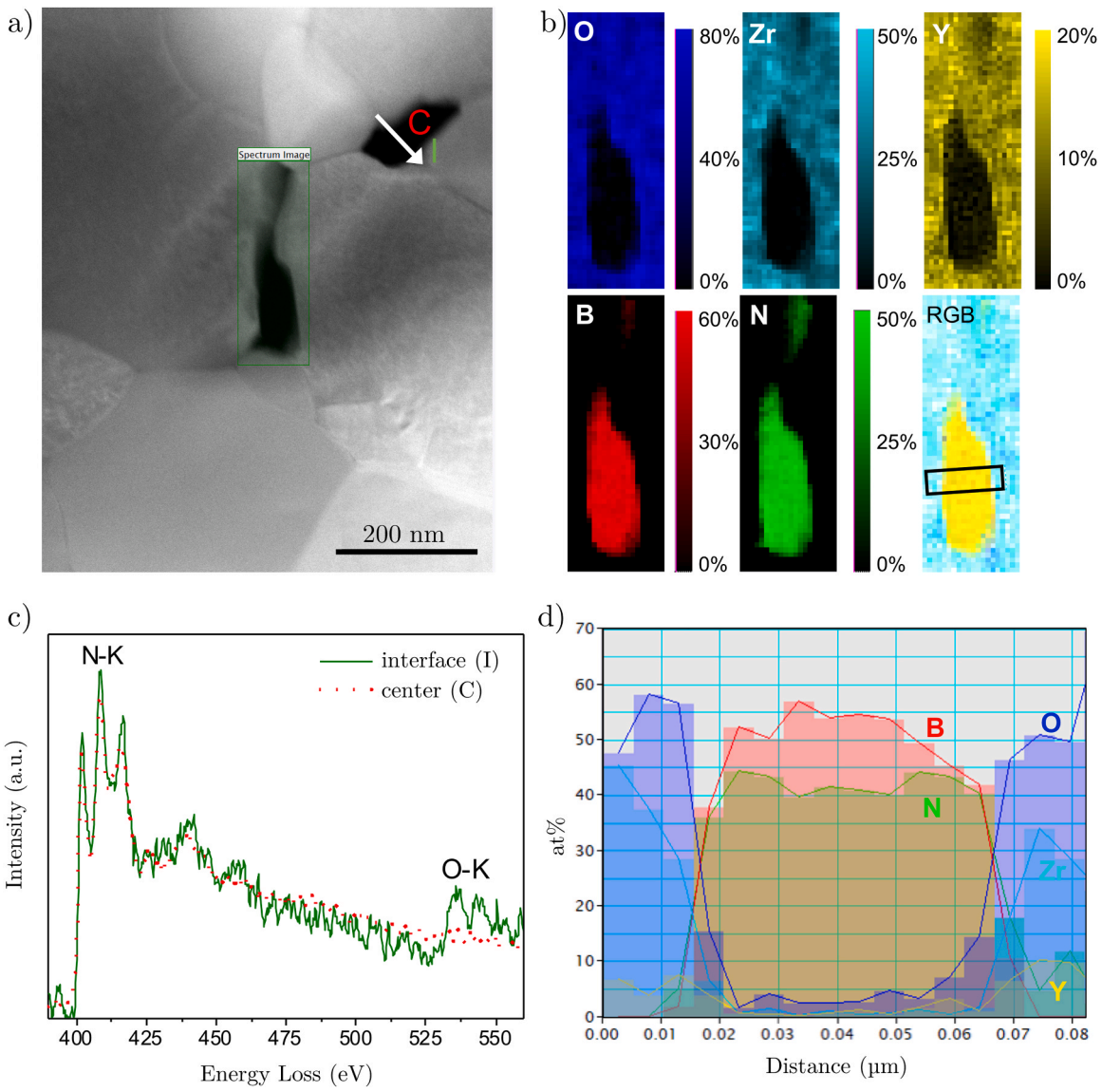

Fig. 8. a) HAADF-STEM micrograph of the Z-2.5B-1250 composite and b) X-EDS elemental maps of the squared region in a). c) EELS spectra over the center (red dotted line) and at the interface (green line) of the upper nanosheet of the micrograph in a). d) Compositional profiles along the BNNS thickness (marked area in the RGB map in b)).

Table 2). So, it is plausible that the BN nanosheets could be hindering the SCG in the matrix.

To determine the influence of the BNNS on the slow crack growth of the zirconia matrix, the R-curve of the composite was assessed on oil-impregnated SEVNB specimens (Fig. 9). Surprisingly, the isolation of the crack tip from the environmental humidity did not change the resulting R-curve, which showed equal toughness at the onset of crack propagation than its analogous in air. Thus, the BN nanosheets must be restraining the water molecules from reaching the zirconia matrix, hindering its stress-corrosion. The shape of the R-curve also remained unchanged, suggesting that the BN nanosheets were not deteriorated by the presence of water either.

The hydrophobic nature of h-BN [38] and the O_2 and H_2O barrier properties [27,54] of the nanosheets seem to be responsible for the SCG inhibition in this composites. Lee et al. [6] studied the hydrothermal degradation of alumina toughened zirconia composites containing 1.5 vol% BNNS, corroborating a minimized tetragonal to monoclinic (t-m) transformability of the matrix. The increased aging resistance was attributed to the presence of BNNS at the grain boundaries, which block the water molecules preventing their penetration into the ceramic [6]. In the composite here analyzed, the nanosheets were distributed throughout the 3Y-TZP matrix with a preferential orientation: the *ab* plane perpendicular to the SPS pressing axis. The SEVNB specimens used for the three-point bending tests were prepared with the notch parallel to the SPS pressing axis (Fig. 1). Hence, as the crack front advances parallel to this axis, the crack tip line encounters the BNNS basal plane. Any water molecule attempting to reach deeper would be blocked by the nanosheets. Although BNNS are known to be good water barriers, this is the first time that inhibition of slow crack growth in a 3Y-TZP matrix by the introduction of BN nanosheets has been demonstrated.

Hence, the intrinsic toughness of the composite containing BNNS is that of the 3Y-TZP matrix, since the observed crack tip toughening is the result of the SCG restraining.

3.4.2. *Evaluation of the extrinsic toughening mechanisms*

The introduction of the hydroxylated BNNS as filler to the 3Y-TZP composite promotes toughening, evidenced by a rising R-curve. Among the extrinsic mechanisms that could be taking part in the toughening of the composite, stress induced t-m zirconia phase transformation and crack bridging by the second phase usually induce the

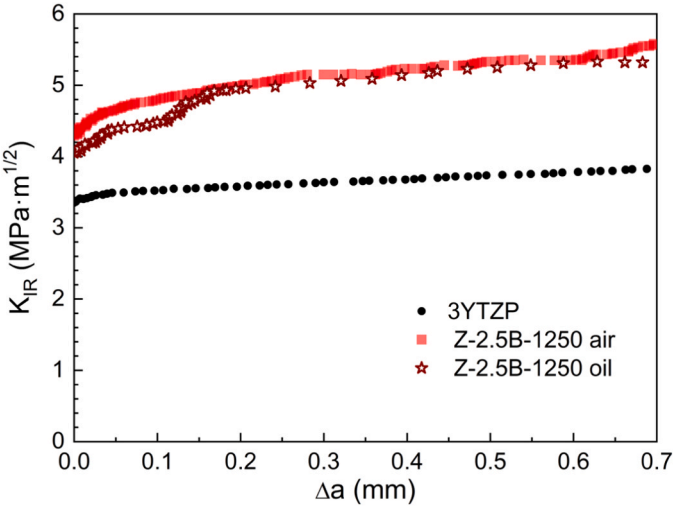

Fig. 9. Crack growth resistance curves of the reference 3Y-TZP (black dots) and the Z-2.5B-1250 composite evaluated in air (plain squares) and on olive oil impregnated specimens (empty stars).

greatest reinforcement [55]. Evaluation of the aforementioned mechanisms could give an insight into the microstructural features that actually cause such toughening.

The monoclinic content on the fracture surface of the composite after failure was ~ 9 vol%, similarly to the monoclinic content detected on the polished surfaces (see section S4), meaning that no further transformation occurred during crack propagation. Hence, the t-m transformation of the 3Y-TZP matrix cannot be responsible for the detected increase in crack growth resistance with crack extension and other mechanisms should be considered.

The SEM micrographs of the composite fracture surfaces after the SEVNB tests revealed that the addition of BNNS increased the roughening of the surface, indicating crack deflection during the propagation (Fig. S8 of the Supplementary Information), a less reinforcing mechanism than phase transformation or bridging [55] which may be also occurring as a way for the crack to pursue lower-energy paths through weaker interfaces [56–60].

Toughening in composites with 2D nanomaterials is generally related to crack bridging. Inspection of the crack paths on the composite polished surface confirmed the occurrence of different mechanisms attending to the size of the BNNS stackings (Fig. 10a – d). Extensive bridging was observed all along the fissure, with the BN nanosheets "gluing" the crack walls together (Fig. 10a and b). The separation between the crack walls (~ 1 μm) suggests that bridging was only promoted by large BNNS (Fig. 10b), whereas smaller nanosheets pull-out from the zirconia matrix (Fig. 10c). The in-situ SEM observation of a stable crack propagating in a rGO/Si_3N_4 composite [12] reached similar conclusions: only small rGO pulled-out in a classical way since high aspect ratio nanosheets were firmly attached to the matrix due to their corrugation. Some holes (marked by the orange arrows in Fig. 10b) also seem to have appeared during bridging, pointing to the breakage of the nanosheets as they stretch during crack opening, rather than sliding out of their matrix socket. This suggests that the nanosheet anchoring to the matrix is stronger than its in-plane resistance. Ramírez et al. [12] also observed the breakage of rGO nanosheets in rGO/silicon nitride composites during SEM in-situ observation of stable cracks, and it was related to the strong cohesion of the nanosheet to the matrix [12]. However, the TEM study in section §3.3 revealed defects (dislocations and holes) on some of the BNNS that could be leading to the early fracture of some nanosheets. Some crack branching and deflection were also detected along the fissure in the composite of the current study (Fig. 10b) as energy dissipating mechanisms, but their appearance was very limited. Finally, the presence of large agglomerates provided a low energy pathway for the crack, which deflected contouring the stacked BNNS (Fig. 10c), as the weak Van der Waal forces assembling the h-BN particles are easily overcome. In spite of this fact, the BNNS promoted a rising R-curve in the composite.

Crack bridging was the most frequent toughening mechanism observed in the composite. This mechanism should only be effective if the energy consumed to de-attach the nanosheets from the matrix was larger than the crack propagation energy. A strong anchoring of the reinforcement to the matrix can be attained by chemical or physical interaction, namely strong chemical bonding or elevated friction/clamping between both phases.

Even though a good chemical bonding was suggested as responsible for the bridging in ceramic composites reinforced with graphene-based nanomaterials (GBN) [12–14,19], the graphene/matrix interfaces were not systematically evaluated. Regarding BNNS composites, a HR-TEM analysis on Si_3N_4/BNNS composites [2] also suggested that the bonding between BNNS and neighboring Si_3N_4 grains was much stronger than the bonding between the individual h-BN layers in BNNS, as revealed by the delamination of the h-BN layers inside the BNNS due to residual stresses in the sample. Nevertheless, no intergranular phase or diffusion layer was observed at the interface between Si_3N_4 grains and BNNS located at the grain boundaries. The microstructural characterization of the composite in the present work evidenced that most nanosheets presented abrupt interfaces with the matrix (section §3.3), despite the in-situ reduction of the partly hydroxylated BNNS during SPS. Hence, no strong chemical interaction can be assumed in this material. In addition to the chemical bonding, the corrugation and wrinkles of high aspect ratio graphene nanosheets are also thought to be responsible of the toughening in GBN/ceramic composites [12,19]. The flexible nature of thin GBN allows their accommodation surrounding ceramic grains, which increases the friction at the interfaces due to the GBN clamping. Nevertheless, the BNNS in this work were observed as rigid platelets that can even limit grain growth, promoting flattened ceramic grains (Fig. 3). Since h-BN is known for its lubricant properties, the nanosheets over such flat ceramic surfaces would easily glide out of the matrix socket during bridging. Thus, no strong physical interaction between the 3Y-TZP matrix and the BN nanosheets would be expected.

According to the microstructural features discussed, none of the mechanisms typically attributed to be at the origin of toughening in ceramic composites reinforced with 2D nanostructures – chemical bonding and nanosheets clamping – should be acting in the composite of the present study. However, although no effective bridging is expected, the Z-2.5B-1250 composite presents an increasing crack growth resistance of $\Delta K_{IR,th} \approx 1$ MPa·m$^{1/2}$. Similar toughening ($\Delta K_{IR,th} \approx 1$ MPa·m$^{1/2}$) was also attained in high aspect ratio rGO reinforced zirconia (3Y-TZP [13] or 8Y-SCZ [14]) composites. All these facts point to the occurrence of another mechanism responsible for the crack bridging toughening, closely related to the nanosheet dimensions. The larger surface area of the high aspect ratio nanosheets should be somehow interacting with the ceramic matrix. The low stacking order and large surface area of high aspect ratio nanosheets make them prone to larger frictional forces with the matrix. Moreover, the nanostructures inside the ceramic composites are found under compression due to the thermal expansion coefficient mismatch during sintering, as proven for composites incorporating graphene-based nanostructures [61,62], thus increasing the friction with the matrix. A more thorough study on the frictional properties between 2D nanostructures and ceramic materials is suggested to unravel the real mechanisms behind the toughening in these composites.

4. Conclusions

BNNS with excellent structural integrity were successfully exfoliated by a simple hydroxide-assisted planetary ball milling procedure. Mostly thin BNNS with 9 – 15 h-BN layers were obtained and thicker particles of up to 40 – 60 h-BN were also observed. The partial hydroxylation of the nanosheets, revealed by XPS, allowed stable suspension in aqueous

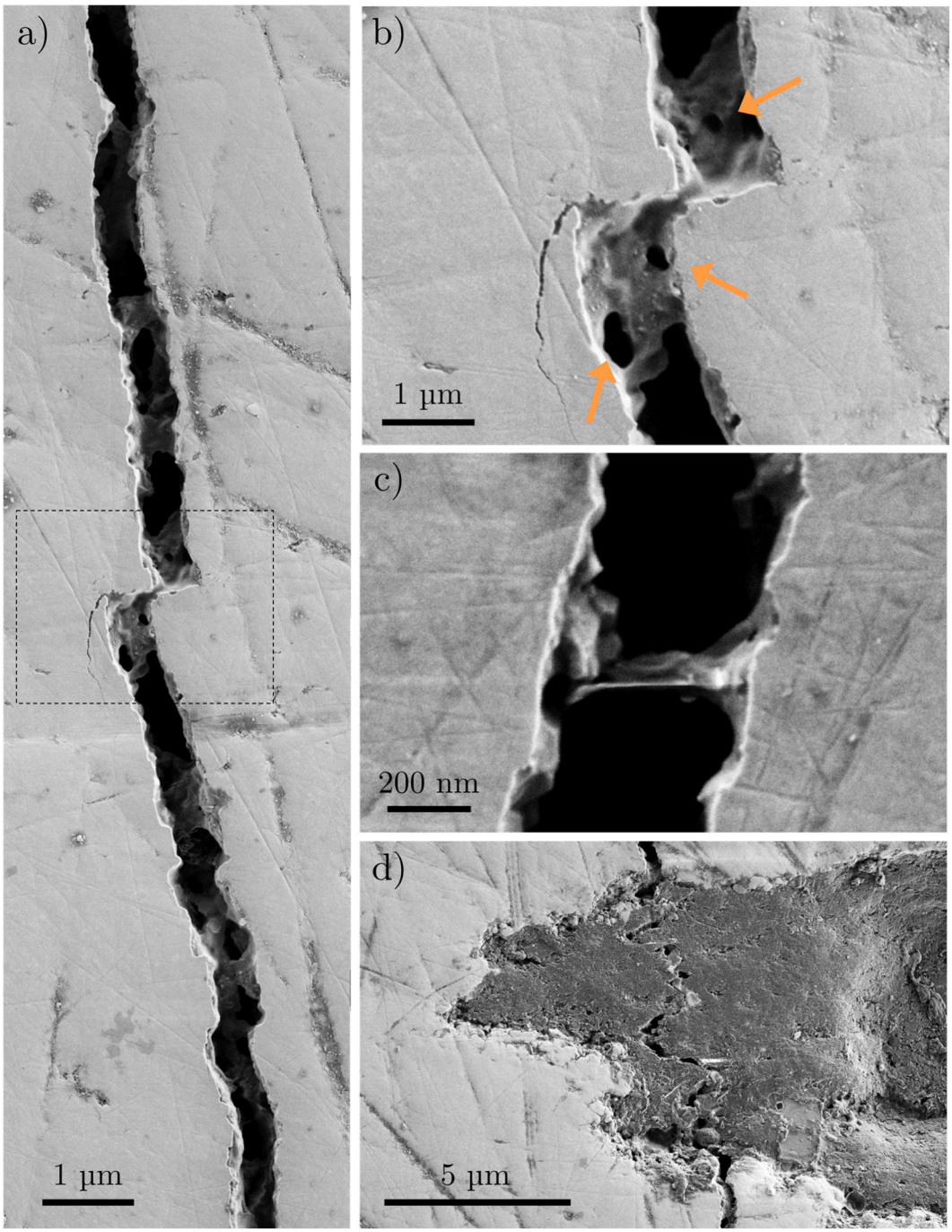

Fig. 10. - SEM inspection of the crack paths after R-curve measurements of the composite Z-2.5B-1250 showing different toughening mechanisms: a) extensive bridging along the crack path, b) crack branching and deflection accompanying the crack bridging (enlarged from the squared area in a)); c) BNNS pull-out; and d) delamination of large BNNS agglomerates. The orange arrows in b) indicate defects on the bridging nanosheets.

Table 2
Mechanical properties of the composite with BNNS and the reference 3Y-TZP: hardness, Young's modulus, SEVNB fracture toughness, crack tip toughness, R-curve toughening and monoclinic volume fraction on fracture surface.

Sample	H_V (GPa)	E (GPa)	K_{IC} (MPa·m$^{1/2}$)	K_{I0} (MPa·m$^{1/2}$)	$\Delta K_{IR,th}$ (MPa·m$^{1/2}$)	$V_{m,f}$ (vol %)
3Y-TZP	13.7 ± 0.1	205 ± 1	4.2 ± 0.1	3.3 ± 0.1	0.3	0.8
Z-2.5B-1250	12.0 ± 0.3	201 ± 1	4.3 ± 0.1	4.2 ± 0.1	1.1	9.1

solutions due to the interaction between -OH groups and water molecules.

Fully dense 3Y-TZP composites with 2.5 vol% BNNS obtained by spark plasma sintering (1250, 1300 and 1350 °C) presented homogeneous distribution of pure and almost completely in-situ reduced nanosheets according to X-EDS. Although most BNNS presented a preferential alignment -perpendicular to the pressing axis during sintering-, randomly oriented nanosheets were also found at a smaller scale. EELS confirmed that the BNNS in the composites retained the highly oriented hexagonal structure even after SPS.

A glassy phase was found at triple junctions, favored by rising sintering temperature, producing an increase in the grain size and a

widening in the grain size distribution. This phase can be attributed to Al and Si impurities from the BNNS and metal oxide traces from the 3Y-TZP powder. The incorporation of partly hydroxylated BNNS and their in-situ reduction during the SPS did not promote the formation of BN-zirconia interphases, observing in most cases abrupt transitions at the 3Y-TZP/BNNS interface.

Although flat and abrupt BNNS/3Y-TZP interfaces are not expected to promote effective bridging, the composite sintered at 1250 ºC presented a rising R-curve behavior of 1 $MPa{\cdot}m^{1/2}$ originated by bridging mechanisms when the crack plane propagated perpendicularly to the BNNS main plane. The incorporation of these BNNS to the 3Y-TZP composite also promoted a 30 % improvement in the crack growth resistance onset compared to the monolithic zirconia probably due to the effectiveness of the BNNS in preventing water molecules from reaching zirconia crack tip.

Summary of novel conclusions

The main conclusions of this work are:

- The spark plasma sintering of the 3Y-TZP composites incorporating hydroxylated boron nitride nanosheets (BNNS) completely achieved the in-situ reduction of the nanostructures at the three evaluated temperatures without the formation of intermediate phases at the zirconia-BN interfaces.
- The BNNS hexagonal structure was retained after the sintering process, presenting a preferential alignment at the mesoscale.
- The introduction of BNNS in the zirconia composite inhibited the stress-corrosion of the zirconia matrix, promoting an increase in the crack growth resistance onset, and induced effective crack bridging resulting in a rising R-curve.

CRediT authorship contribution statement

C. Muñoz-Ferreiro: Investigation, Visualization, Writting – original draft. **H. Reveron:** Conceptualization, Investigation, Visualization, Writing – review & editing, Supervision. **T.C. Rojas:** Investigation, Visualization, Writing – review & editing. **D.F. Reyes:** Investigation, Writing –- review & editing. **S. Cottrino:** Investigation, Writing – review & editing. **P. Moreno:** Investigation, Writing – review & editing. **J. Prada-Rodrigo:** Investigation, Writing – review & editing. **A. Morales-Rodríguez:** Conceptualization, Writing – review & editing, Funding acquisition. **J. Chevalier:** Conceptualization, Writing – review & editing, Supervision. **Á. Gallardo-López:** Conceptualization, Writing – review & editing, Supervision, Project administration, Funding acquisition. **R. Poyato:** Conceptualization, Writting – original draft, Writing – review & editing, Supervision, Project administration, Funding acquisition.

Declaration of Competing Interest

The authors declare that they have no known competing financial interests or personal relationships that could have appeared to influence the work reported in this paper.

Acknowledgements

This research was supported by projects PGC2018–101377-B-100 and PID2022–140191NB-I0 funded by MCIN/AEI/ 10.13039/501100011033 (Ministerio de Ciencia e Innovación, Spanish Government, Agencia Estatal de Investigación) and by ERDF (European Regional Development Funding) “A way of making Europe”, and by project P20_01024 (Junta de Andalucía/FEDER, UE 2014–2020). C. Muñoz-Ferreiro acknowledges the financial support of a VI PPIT-US (Plan Propio Universidad de Sevilla, Spain) fellowship through the contract USE-18740-H. Daniel F. Reyes would like to thank the University of Cádiz and the Ministry of Universities for the award of the grant “Recualificación del Profesorado” (UCA/R155REC/2021), funded by the Ministry of Universities of the Spanish Government through the European Recovery Instrument (Order UNI/551/2021). We would also like to thank the central services of the University of Cádiz (DME-SC-ICyT-ELECMI-UCA) for the support offered to obtain the TEM measurements. P. Moreno and J. Prada-Rodrigo also acknowledge the support of Ministerio de Ciencia e Innovación (PID2020-119003GB-I00).

Appendix A. Supporting information

Supplementary data associated with this article can be found in the online version at doi:10.1016/j.jeurceramsoc.2024.02.002.

References

[1] B. Lee, D. Lee, J.H. Lee, H.J. Ryu, S.H. Hong, Enhancement of toughness and wear resistance in boron nitride nanoplatelet (BNNP) reinforced Si_3N_4 nanocomposites, Sci. Rep. 6 (2016) 27609, https://doi.org/10.1038/srep27609.

[2] M. Tatarková, P. Tatarko, A. Kovalčíková, I. Dlouhý, J. Dusza, P. Šajgalík, Influence of hexagonal boron nitride nanosheets on phase transformation, microstructure evolution and mechanical properties of Si_3N_4 ceramics, J. Eur. Ceram. Soc. 41 (2021) 5115–5126, https://doi.org/10.1016/j.jeurceramsoc.2021.01.057.

[3] X. Yang, J. Bi, G. Liang, Y. Li, L. Meng, C. Wu, X. Zhang, The effect of boron nitride nanosheets on the mechanical and thermal properties of aluminum nitride ceramics, Int. J. Appl. Ceram. Technol. 19 (2022) 2817–2825, https://doi.org/10.1111/ijac.14069.

[4] H. Jiang, N. Ding, Z.-Y. Zou, X.-H. Wang, W.-Z. Lu, Flexural strength, thermal and dielectric properties of AlN ceramics with BN nanoplatelets addition, Ceram. Int. 48 (2022) 19250–19257, https://doi.org/10.1016/j.ceramint.2022.03.217.

[5] Z. Yin, J. Bi, G. Liang, L. Qiao, Y. Yang, J. Gao, S. Wang, H. Wang, Microstructure and mechanical properties of boron nitride nanosheets reinforced eutectic-composition Al_2O_3/YAG/YSZ composites, Mater. Charact. 196 (2023) 112631, https://doi.org/10.1016/j.matchar.2022.112631.

[6] B. Lee, J.-S. Kwon, M.W. Khalid, K.-M. Kim, J. Kim, K.M. Lim, S.H. Hong, Boron nitride nanoplatelets as reinforcement material for dental ceramics, Dent. Mater. 36 (2020) 744–754, https://doi.org/10.1016/j.dental.2020.03.002.

[7] L.H. Li, J. Cervenka, K. Watanabe, T. Taniguchi, Y. Chen, Strong oxidation resistance of atomically thin boron nitride nanosheets, ACS Nano 8 (2014) 1457–1462, https://doi.org/10.1021/nn500059s.

[8] D. Golberg, Y. Bando, Y. Huang, T. Terao, M. Mitome, C. Tang, C. Zhi, Boron nitride nanotubes and nanosheets, ACS Nano 4 (2010) 2979–2993, https://doi.org/10.1021/nn1006495.

[9] Y. Shi, C. Hamsen, X. Jia, K.K. Kim, A. Reina, M. Hofmann, A.L. Hsu, K. Zhang, H. Li, Z.-Y. Juang, MildredS. Dresselhaus, L.-J. Li, J. Kong, Synthesis of few-layer hexagonal boron nitride thin film by chemical vapor deposition, Nano Lett. 10 (2010) 4134–4139, https://doi.org/10.1021/nl1023707.

[10] G. Sun, J. Bi, W. Wang, J. Zhang, Enhancing mechanical properties of fused silica composites by introducing well-dispersed boron nitride nanosheets, Ceram. Int. 44 (2018) 5002–5009, https://doi.org/10.1016/j.ceramint.2017.12.096.

[11] W. Wang, G. Sun, Y. Chen, X. Sun, J. Bi, Preparation and mechanical properties of boron nitride nanosheets/alumina composites, Ceram. Int. 44 (2018) 21993–21997, https://doi.org/10.1016/j.ceramint.2018.08.314.

[12] C. Ramírez, Q. Wang, M. Belmonte, P. Miranzo, M. Isabel Osendi, B.W. Sheldon, N. P. Padture, Direct in situ observation of toughening mechanisms in nanocomposites of silicon nitride and reduced graphene-oxide, Scr. Mater. 149 (2018) 40–43, https://doi.org/10.1016/j.scriptamat.2018.02.004.

[13] C. López-Pernía, C. Muñoz-Ferreiro, J. Prada-Rodrigo, P. Moreno, H. Reveron, J. Chevalier, A. Morales-Rodríguez, R. Poyato, Á. Gallardo-López, R-curve evaluation of 3YTZP/graphene composites by indirect compliance method, J. Eur. Ceram. Soc. 43 (2023) 3486–3497, https://doi.org/10.1016/j.jeurceramsoc.2023.02.002.

[14] A. Gómez-Gómez, C. Ramírez, J. Llorente, A. Garcia, P. Moreno, H. Reveron, J. Chevalier, M.I. Osendi, M. Belmonte, P. Miranzo, Improved crack resistance and thermal conductivity of cubic zirconia containing graphene nanoplatelets, J. Eur. Ceram. Soc. 40 (2020) 1557–1565, https://doi.org/10.1016/j.jeurceramsoc.2019.12.016.

[15] O.T. Picot, V.G. Rocha, C. Ferraro, N. Ni, E. D'Elia, S. Meille, J. Chevalier, T. Saunders, T. Peijs, M.J. Reece, E. Saiz, Using graphene networks to build bioinspired self-monitoring ceramics, Nat. Commun. 8 (2017) 14425, https://doi.org/10.1038/ncomms14425.

[16] A.H. De Aza, J. Chevalier, G. Fantozzi, M. Schehl, R. Torrecillas, Crack growth resistance of alumina, zirconia and zirconia toughened alumina ceramics for joint prostheses, Biomaterials 23 (2002) 937–945, https://doi.org/10.1016/S0142-9612(01)00206-X.

[17] K. Markandan, J.K. Chin, M.T.T. Tan, Recent progress in graphene based ceramic composites: a review, J. Mater. Res. 32 (2017) 84–106, https://doi.org/10.1557/jmr.2016.390.

[18] O. Tapasztó, V. Puchy, Z.E. Horváth, Z. Fogarassy, E. Bódis, Z. Károly, K. Balázsi, J. Dusza, L. Tapasztó, The effect of graphene nanoplatelet thickness on the fracture

toughness of Si_3N_4 composites, Ceram. Int. 45 (2019) 6858–6862, https://doi.org/10.1016/j.ceramint.2018.12.180.
[19] Q. Wang, C. Ramírez, C.S. Watts, O. Borrero-López, A.L. Ortiz, B.W. Sheldon, N. P. Padture, Fracture, fatigue, and sliding-wear behavior of nanocomposites of alumina and reduced graphene-oxide, Acta Mater. 186 (2020) 29–39, https://doi.org/10.1016/j.actamat.2019.12.035.
[20] G. Liang, G. Sun, J. Bi, W. Wang, X. Yang, Y. Li, Mechanical and dielectric properties of functionalized boron nitride nanosheets/silicon nitride composites, Ceram. Int. 47 (2021) 2058–2067, https://doi.org/10.1016/j.ceramint.2020.09.038.
[21] P. Tatarko, S. Grasso, Z. Chlup, H. Porwal, M. Kašiarová, I. Dlouhý, M.J. Reece, Toughening effect of multi-walled boron nitride nanotubes and their influence on the sintering behaviour of 3Y-TZP zirconia ceramics, J. Eur. Ceram. Soc. 34 (2014) 1829–1843, https://doi.org/10.1016/j.jeurceramsoc.2013.12.046.
[22] C.H. Kim, E.B. Go, H. Tae Kim, Thermophysical properties of zirconia toughened alumina ceramics with boron nitride nanotubes addition, Heat. Transf. Eng. 41 (2020) 1354–1364, https://doi.org/10.1080/01457632.2019.1628484.
[23] C. Ramirez, P. Miranzo, M. Belmonte, M.I. Osendi, P. Poza, S.M. Vega-Diaz, M. Terrones, Extraordinary toughening enhancement and flexural strength in Si_3N_4 composites using graphene sheets, J. Eur. Ceram. Soc. 34 (2014) 161–169, https://doi.org/10.1016/j.jeurceramsoc.2013.08.039.
[24] C. Muñoz-Ferreiro, A. Morales-Rodríguez, Á. Gallardo-López, R. Poyato, A first insight into the microstructure and crack propagation in novel boron nitride nanosheet/3YTZP composites, Bol. Soc. Esp. Cerám. y Vidr. 60 (2021) 128–136, https://doi.org/10.1016/j.bsecv.2020.02.003.
[25] Z. Zeng, Y. Liu, W. Chen, X. Li, Q. Zheng, K. Li, R. Guo, Fabrication and properties of in situ reduced graphene oxide-toughened zirconia composite ceramics, J. Am. Ceram. Soc. 101 (2018) 3498–3507, https://doi.org/10.1111/jace.15483.
[26] K.-G. Zhou, N.-N. Mao, H.-X. Wang, Y. Peng, H.-L. Zhang, A mixed-solvent strategy for efficient exfoliation of inorganic graphene analogues, Angew. Chem. Int. Ed. 50 (2011) 10839–10842, https://doi.org/10.1002/anie.201105364.
[27] D. Lee, B. Lee, K.H. Park, H.J. Ryu, S. Jeon, S.H. Hong, Scalable exfoliation process for highly soluble boron nitride nanoplatelets by hydroxide-assisted ball milling, Nano Lett. 15 (2015) 1238–1244, https://doi.org/10.1021/nl504397h.
[28] R.C. Garvie, P.S. Nicholson, Phase analysis in zirconia systems, J. Am. Ceram. Soc. 55 (1972) 303–305, https://doi.org/10.1111/j.1151-2916.1972.tb11290.x.
[29] H. Toraya, M. Yoshimura, S. Somiya, Calibration curve for quantitative analysis of the monoclinic-tetragonal ZrO_2 system by X-ray diffraction, J. Am. Ceram. Soc. 67 (1984) C-119–C-121, https://doi.org/10.1111/j.1151-2916.1984.tb19715.x.
[30] ASTM E 1876 - 01, Standard test method for dynamic Young's modulus, shear modulus, and Poisson's ratio by impulse excitation of vibration, ASTM International,, PA, USA, 2001.
[31] M. Turon-Vinas, M. Anglada, Fracture toughness of zirconia from a shallow notch produced by ultra-short pulsed laser ablation, J. Eur. Ceram. Soc. 34 (2014) 3865–3870, https://doi.org/10.1016/j.jeurceramsoc.2014.05.009.
[32] H.D. Carlton, J.W. Elmer, D.C. Freeman, R.D. Schaeffer, O. Derkach, G.F. Gallegos, Laser notching ceramics for reliable fracture toughness testing, J. Eur. Ceram. Soc. 36 (2016) 227–234, https://doi.org/10.1016/j.jeurceramsoc.2015.08.021.
[33] M. Turon-Vinas, J. Morillas, P. Moreno, M. Anglada, Evaluation of damage in front of starting notches induced by ultra-short pulsed laser ablation for the determination of fracture toughness in zirconia, J. Eur. Ceram. Soc. 37 (2017) 5127–5131, https://doi.org/10.1016/j.jeurceramsoc.2017.07.006.
[34] ASTM C1421 - 10, "Standard test methods for determination of fracture toughness of advanced ceramics at ambient temperature, ASTM International,, PA, USA, 2010.
[35] D. Munz, T. Fett (Eds.), Ceramics: Mechanical Properties, Failure Behaviour, Materials Selection, Springer Berlin Heidelberg, Berlin, Heidelberg, 1999, https://doi.org/10.1007/978-3-642-58407-7.
[36] ASTM C373-18, Standard test methods for determination of water absorption and associated properties by vacuum method for pressed ceramic tiles and glass tiles and boil method for extruded ceramic tiles and non-tile fired ceramic whiteware products, ASTM International,, PA, USA, 2018.
[37] J. Chevalier, C. Olagnon, G. Fantozzi, Subcritical crack propagation in 3Y-TZP ceramics: static and cyclic fatigue, J. Am. Ceram. Soc. 82 (1999) 3129–3138, https://doi.org/10.1111/j.1151-2916.1999.tb02213.x.
[38] T. Sainsbury, A. Satti, P. May, Z. Wang, I. McGovern, Y.K. Gun'ko, J. Coleman, Oxygen radical functionalization of boron nitride nanosheets, J. Am. Chem. Soc. 134 (2012) 18758–18771, https://doi.org/10.1021/ja3080665.
[39] A. Nag, K. Raidongia, K.P.S.S. Hembram, R. Datta, U.V. Waghmare, C.N.R. Rao, Graphene analogues of BN: novel synthesis and properties, ACS Nano 4 (2010) 1539–1544, https://doi.org/10.1021/nn9018762.
[40] C. López-Pernía, C. Muñoz-Ferreiro, C. González-Orellana, A. Morales-Rodríguez, Á. Gallardo-López, R. Poyato, Optimizing the homogenization technique for graphene nanoplatelet/yttria tetragonal zirconia composites: influence on the microstructure and the electrical conductivity, J. Alloy. Compd. 767 (2018) 994–1002, https://doi.org/10.1016/j.jallcom.2018.07.199.
[41] L. Gremillard, T. Epicier, J. Chevalier, G. Fantozzi, Effect of cooling rate on the location and chemistry of glassy phases in silica-doped 3Y-TZP ceramics, J. Eur. Ceram. Soc. 25 (2005) 875–882, https://doi.org/10.1016/j.jeurceramsoc.2004.03.032.
[42] S. Turan, C.A. Davis, K.M. Knowles, Orientation dependence of EELS spectra from hexagonal boron nitride, J. Phys. Conf. Ser. (1995) 63–66.
[43] J.-J. Xu, Y.-J. Bai, W.-L. Wang, S.-R. Wang, F.-D. Han, Y.-X. Qi, J.-Q. Bi, Toughening and reinforcing zirconia ceramics by introducing boron nitride nanotubes, Mater. Sci. Eng.: A 546 (2012) 301–306, https://doi.org/10.1016/j.msea.2012.03.077.
[44] W.-F. Ho, H.-C. Hsu, Y.-F. Peng, S.-C. Wu, Microstructure and mechanical properties of dental 3Y-TZP ceramics by using $CaO–P_2O_5$ glass as additive, Ceram. Int. 37 (2011) 1169–1174, https://doi.org/10.1016/j.ceramint.2010.11.027.
[45] Y. Sun, Y. Zhang, J. Guo, Microstructure and bending strength of 3Y-TZP ceramics by liquid-phase sintering with CAS addition, Ceram. Int. 29 (2003) 229–232, https://doi.org/10.1016/S0272-8842(02)00097-4.
[46] H.T. Kim, C.H. Kim, E.B. Go, Thermal properties of zirconia toughened alumina ceramics with boron nitride nanotubes, 13th Intern. Conf. Heat Transfer, Fluid Mechn. and Thermod. (2017) 275–280.
[47] T.P. Nguyen, Z. Hamidzadeh Mahaseni, M. Dashti Germi, S.A. Delbari, Q.V. Le, Z. Ahmadi, M. Shokouhimehr, M. Shahedi Asl, A. Sabahi Namini, Densification behavior and microstructure development in TiB_2 ceramics doped with h-BN, Ceram. Int. 46 (2020) 18970–18975, https://doi.org/10.1016/j.ceramint.2020.04.223.
[48] M. Dashti Germi, Z. Hamidzadeh Mahaseni, Z. Ahmadi, M. Shahedi Asl, Phase evolution during spark plasma sintering of novel Si_3N_4-doped TiB_2–SiC composite, Mater. Charact. 145 (2018) 225–232, https://doi.org/10.1016/j.matchar.2018.08.043.
[49] M. Tatarková, P. Tatarko, P. Šajgalík, Si_3N_4 ceramics, structure and properties, in: M. Pomeroy (Ed.), Encyclopedia of Materials: Technical Ceramics and Glasses, Elsevier, Oxford, 2021, pp. 109–118, https://doi.org/10.1016/B978-0-12-818542-1.00021-7.
[50] L. Gremillard, T. Epicier, J. Chevalier, G. Fantozzi, Microstructural study of silica-doped zirconia ceramics, Acta Mater. 48 (2000) 4647–4652, https://doi.org/10.1016/S1359-6454(00)00252-4.
[51] Y. Ikuhara, T. Yamamoto, A. Kuwabara, H. Yoshida, T. Sakuma, Structure and chemistry of grain boundaries in SiO_2-doped TZP, Sci. Technol. Adv. Mater. 2 (2001) 411–424, https://doi.org/10.1016/S1468-6996(01)00009-2.
[52] C. Muñoz-Ferreiro, A. Morales-Rodríguez, T.C. Rojas, E. Jiménez-Piqué, C. López-Pernía, R. Poyato, A. Gallardo-López, Microstructure, interfaces and properties of 3YTZP ceramic composites with 10 and 20 vol% different graphene-based nanostructures as fillers, J. Alloy. Compd. 777 (2019) 213–224, https://doi.org/10.1016/j.jallcom.2018.10.336.
[53] J. Eichler, J. Rödel, U. Eisele, M. Hoffman, Effect of grain size on mechanical properties of submicrometer 3Y-TZP: fracture strength and hydrothermal degradation, J. Am. Ceram. Soc. 90 (2007) 2830–2836, https://doi.org/10.1111/j.1551-2916.2007.01643.x.
[54] A.C. Ferrari, F. Bonaccorso, V. Fal'ko, K.S. Novoselov, S. Roche, P. Bøggild, S. Borini, F.H.L. Koppens, V. Palermo, N. Pugno, J.A. Garrido, R. Sordan, A. Bianco, L. Ballerini, M. Prato, E. Lidorikis, J. Kivioja, C. Marinelli, T. Ryhänen, A. Morpurgo, J.N. Coleman, V. Nicolosi, L. Colombo, A. Fert, M. Garcia-Hernandez, A. Bachtold, G.F. Schneider, F. Guinea, C. Dekker, M. Barbone, Z. Sun, C. Galiotis, A.N. Grigorenko, G. Konstantatos, A. Kis, M. Katsnelson, L. Vandersypen, A. Loiseau, V. Morandi, D. Neumaier, E. Treossi, V. Pellegrini, M. Polini, A. Tredicucci, G.M. Williams, B.H. Hong, J.-H. Ahn, J.M. Kim, H. Zirath, B.J. van Wees, H. van der Zant, L. Occhipinti, A.D. Matteo, I.A. Kinloch, T. Seyller, E. Quesnel, X. Feng, K. Teo, N. Rupesinghe, P. Hakonen, S.R.T. Neil, Q. Tannock, T. Löfwander, J. Kinaret, Science and technology roadmap for graphene, related two-dimensional crystals, and hybrid systems, Nanoscale 7 (2015) 4598–4810, https://doi.org/10.1039/C4NR01600A.
[55] F. Zhang, J. Chevalier, C. Olagnon, S. Huang, W. Veulemans, K. Vanmeensel, J. Vleugels, Slow crack growth resistance of electrically conductive zirconia-based composites with non-oxide reinforcements, J. Eur. Ceram. Soc. 39 (2019) 641–646, https://doi.org/10.1016/j.jeurceramsoc.2018.09.034.
[56] J. Liu, H. Yan, K. Jiang, Mechanical properties of graphene platelet-reinforced alumina ceramic composites, Ceram. Int. 39 (2013) 6215–6221, https://doi.org/10.1016/j.ceramint.2013.01.041.
[57] A.G. Sheinerman, Modeling of fracture toughness enhancement and reduction in fully dense ceramic/graphene composites, Eur. J. Mech. - A/Solids 98 (2023) 104891, https://doi.org/10.1016/j.euromechsol.2022.104891.
[58] S.V. Bobylev, A.G. Sheinerman, Effect of crack bridging on the toughening of ceramic/graphene composites, Rev. Adv. Mater. Sci. 57 (2018) 54–62, https://doi.org/10.1515/rams-2018-0047.
[59] L. Liu, Y. Wang, X. Li, L. Xu, X. Cao, Y. Wang, Z. Wang, C. Meng, W. Zhu, X. Ouyang, Enhancing toughness in boron carbide with reduced graphene oxide, J. Am. Ceram. Soc. 99 (2016) 257–264, https://doi.org/10.1111/jace.13943.
[60] I. Ahmad, M. Islam, H.S. Abdo, T. Subhani, K.A. Khalil, A.A. Almajid, B. Yazdani, Y. Zhu, Toughening mechanisms and mechanical properties of graphene nanosheet-reinforced alumina, Mater. Des. 88 (2015) 1234–1243, https://doi.org/10.1016/j.matdes.2015.09.125.
[61] C. Muñoz-Ferreiro, C. López-Pernía, Á. Gallardo-López, R. Poyato, Unravelling the optimization of few-layer graphene crystallinity and electrical conductivity in ceramic composites by Raman spectroscopy, J. Eur. Ceram. Soc. 41 (2021) 290–298, https://doi.org/10.1016/j.jeurceramsoc.2021.09.025.
[62] A. Morales-Rodríguez, C. González-Orellana, A.A. Pérez-García, C. López-Pernía, C. Muñoz-Ferreiro, R. Poyato, Á. Gallardo-López, Ageing-resistant zirconia/graphene-based nanostructures composites for use as biomaterials, J. Eur. Ceram. Soc. 42 (2022) 1784–1795, https://doi.org/10.1016/j.jeurceramsoc.2021.11.060.